3 Characterization of Magnetic Materials by Means of Neutron Scattering

G. Ehlers, F. Klose

3. 1 Introduction

The neutron is an elementary particle with a particular combination of properties that makes it uniquely versatile as a condensed matter probe. These properties are:

(1) It is not electrically charged;

(2) It has spin 1/2 and a magnetic dipole moment of μ_n = -1.913μ_N (with the nuclear magneton μ_N = 5.051×10^{-27} J/T)

(3) It has mass (m_N = 1.675×10^{-27} kg)

The lack of an electric charge has two important consequences. First, since the dominant scattering by electrical charges is absent, in solid matter one can observe neutron scattering processes by atomic nuclei via strong interaction or by magnetic moments via dipolar interaction with the magnetic moment of the neutron. One of the most remarkable features of the neutron scattering technique is that magnetic interaction strengths are often on the same order of magnitude as nuclear interactions such that magnetic and structural properties of the sample can be probed simultaneously. Second, the neutron is able to penetrate deeply into condensed matter (typically a few mm to a few cm) unless there is one of the few isotopes with high absorption cross-section present. The neutron is therefore well suited for the study of true bulk properties of matter.

Magnetic scattering experiments can be performed on a large variety of samples, including, for example, single crystals, powders, and even artificially grown thin film structures. Physical quantities that can be measured by magnetic neutron scattering include (see Sections 3. 2 and 3. 3 for a detailed discussion):

(1) Magnetic structures across various length scales (e.g. ranging from ferro- and antiferromagnetic order at atomic length scales to mesoscopic structures like flux lattices of superconductors, magnetic spirals or magnetic depth profiles in thin films);

(2) Magnetization density (e.g. how the moment is distributed in the vicinity of magnetic atoms);

(3) Magnetic excitations (e.g. spin waves).

In many cases the obtained information is unique, i.e. it cannot be derived by means of other experimental techniques.

Neutron beams are produced in research reactors by nuclear fission (for example at the Institute Laue-Langevin (ILL), Grenoble, France, see www.ill.fr) or in spallation sources by using linear proton accelerators (for example at ISIS at the Rutherford Appleton Lab, Oxford, Great Britain, see www.isis.rl.ac.uk, or at the US Spallation Neutron Source (SNS), see www.sns.anl.gov). Although neutron scattering is an intensity-limited technique (see Section 3. 1. 1) one can obtain sufficient intensity (at today's best sources typically 10^6-10^7 neutrons cm^{-2}s^{-1} on the sample) to do experiments. The neutron has mass and this has the important consequence that neutrons created by these processes can be efficiently slowed down (moderated) by collisions with light atoms to specific energy ranges that are favorable for particular condensed matter studies. The energy ranges are typically labeled according to the temperature of the moderator material. Heated graphite blocks (T > 2000 K) deliver "hot" neutrons, room-temperature water moderators deliver "thermal" neutrons, and liquid hydrogen moderators (T < 30 K) are used for "cold" neutron production. The relation between the neutron kinetic energy and (via de-Broglie) its wavelength is

$$E = \frac{p^2}{2m} = \frac{h^2}{2m\lambda^2}$$

$$E(\text{meV}) = \frac{81.8042}{[\lambda(\text{Å})]^2} \ .$$

Thus, typical ranges for neutron energies and corresponding wavelengths used in neutron scattering experiments are (approx.):

(1) "hot" neutrons E is 100-500 meV, λ is 0.5-1 Å;
(2) "thermal" neutrons E is 10-100 meV, λ is 1-3 Å;
(3) "cold" neutrons E is 0.1-10 meV, λ is 3-30 Å.

We see that both energy and wavelength are in ranges that are suitable for condensed matter investigations, the wavelength being in the range of typical atomic distances and the energy corresponding to that of lattice vibrations or spin excitations. There is thus a fundamental difference between neutrons and X-rays, where a wavelength of 1 Å corresponds to the energy of 12.4 keV. Neutrons can therefore probe correlations in condensed matter in space (atomic to mesoscopic length scales) and time (10^{-14} s to 10^{-7} s) simultaneously. Figure 3. 1 illustrates some important characteristic length scales for structural and magnetic properties of condensed matter. In scattering experiments, the connection between probed length scale d and neutron wavelength λ is given by Bragg's law: $2 \, d \, \sin\theta = n \, \lambda$, where 2θ is the scattering angle and n is an integer.

The neutron as a free (i.e. unbound) particle is not stable. Currently, the best value for neutron life time is (886.7 ± 1.9) s (Groom et al., 2000).
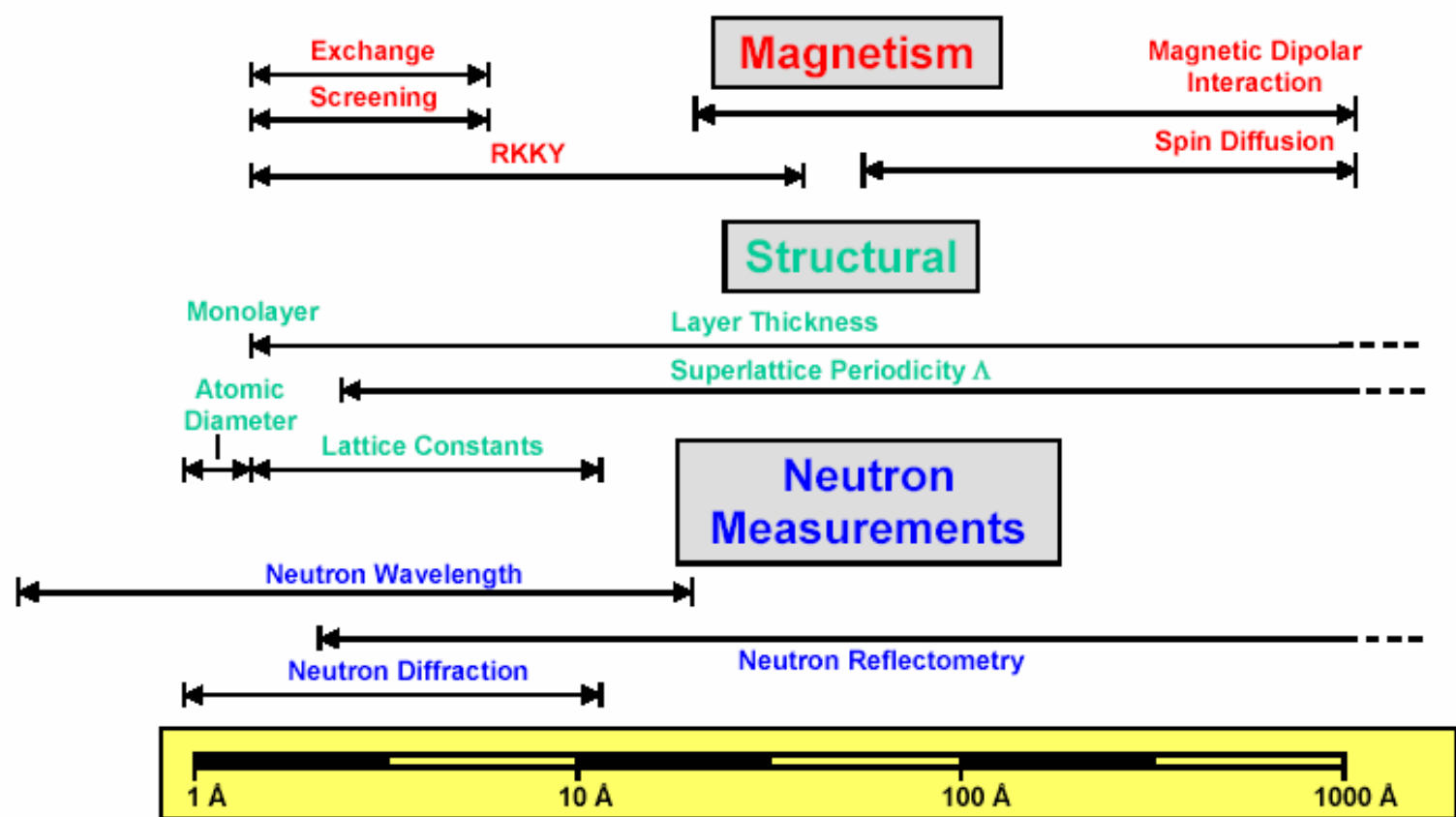
Figure 3. 1   Comparison of characteristic length scales of magnetic and structural properties of matter and length scales that are accessible in typical neutron scattering experiments.

This is, in practice, however, not an issue because the life time is much longer than necessary to do scattering experiments, i.e. the time the neutron spends traveling from the source to the detector.

The intention of our article is to give an overview of basic concepts of magnetic neutron scattering techniques at an introductory level. We will emphasize the experimental aspects and will discuss some recent scientific highlights that illustrate the uniqueness of these techniques. We do not intend, however, to review the scientific progress in this large research field. Our choice is a personal one and the available space is limited, so we will certainly omit some topics which might be of interest to a particular reader. For more details and other aspects of neutron scattering, we refer to introductory texts available in the literature (de Gennes, 1963; Rossat-Mignod, 1987; Mezei, 1991), or to one of the numerous text books on neutron scattering (Squires, 1978; Lovesey, 1984; Williams, 1988; Furrer, 1995;, Shirane et al., 2002).

Our article is organized as follows: In the first section we will briefly discuss the basic magnetic scattering theory (Section 3. 1. 1) and give an introduction to polarized neutron beam instrumentation (Section 3. 1. 2) as well as to polarization analysis (Section 3. 1. 3). Sections 3. 2 and 3. 3 review neutron scattering instruments that are particularly useful for studies on magnetic materials. Section 3. 2 focuses on elastic magnetic scattering and in Section 3. 3 we discuss spectrometers that are specifically designed to measure excitations in magnetic materials. Scientific examples are included for both types of instruments.

3. 1. 1 Cross-Section Formalism

Nuclei, with a typical diameter on the order of femtometers (10^{-15} m), are point-like on the scale of typical neutron wavelengths in the Å-range (10^{-10} m). Therefore the scattering from a fixed nucleus is essentially s-wave scattering and can be described by a single (generally complex) number b, the scattering length. This parameter is known for most isotopes to a precision of a few percent and is on the order of 10^{-13} to 10^{-12} cm (a list of neutron scattering length and cross-sections can be found here: http://www.ncnr.nist.gov/resources/n-lengths/). In comparison, typical b values for X-rays are on the order of 10^{-11} cm, resulting in much stronger interactions in scattering experiments. In contrast to the X-ray case, however, there is no systematic dependence of b on the atomic number Z and nucleon number N. This opens the possibility to study isotope effects. The case of hydrogen and deuterium is of particular importance for soft matter physics. Isotope mixing can also be beneficial in magnetism studies, for example for enhancing the sensitivity for magnetic signals (Hoffmann et al., 2002).

From these numbers one can immediately conclude that typical cross-sections $\sigma = 4\pi b^2$ are small and that, therefore, the scattering process may be treated in first order perturbation theory (Born approximation). This picture breaks down only for a few exceptional cases, for example coherent Bragg scattering from perfect crystallites of dimension $d \approx 10^{-3}$ cm or larger (Mezei, 1991) or grazing incidence techniques like neutron reflectometry (see Section 3. 2. 3).

Due to the relatively small values for the scattering lengths and the correspondingly weak beam-sample interactions, neutron scattering is an intensity-limited technique. This has its consequences in the instrument design, where one often tries to increase intensity by using large detector arrays covering a large solid angle. On the other hand, a convenient corollary is that data are relatively easy to interpret because multiple scattering contributions are usually small.

Magnetic scattering results from the interaction of the neutron spin with the magnetic field generated by the unpaired electrons of the atom. The corresponding magnetization density function may be strongly delocalized, its extent often being comparable in size with typical neutron wavelengths, and generally leading to a decrease of the intensity at high q (see discussion on the form factor $F(q)$ below). Nevertheless, one can define an effective magnetic scattering length p as well, which, for a magnetic moment of $1\mu_B$, amounts to 0.27×10^{-12} cm.

In a neutron scattering experiment one measures a cross-section, that is, the number of neutrons scattered per unit time into a solid angle $d\Omega$ with neutron energy transfer in the interval $(\hbar\omega, \hbar(\omega + d\omega))$, normalized to the incident neutron flux. Figure 3. 2 shows a typical scattering geometry.
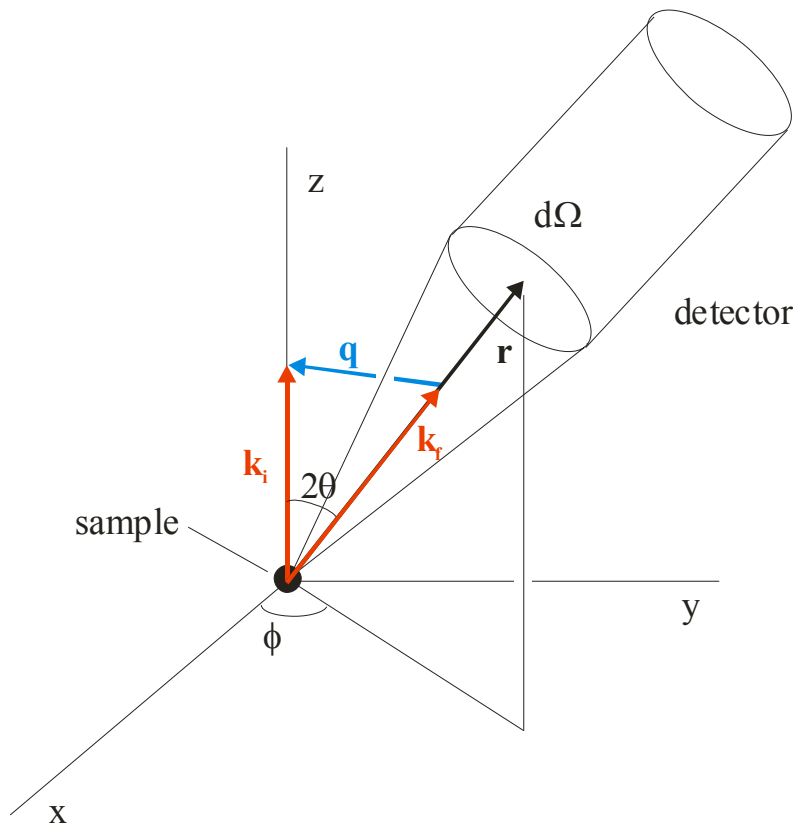
Figure 3. 2   Scattering geometry: The incident neutrons are traveling along the *z* axis and are characterized by their wave vector $\boldsymbol{k_i}$ and energy E_i ($|\boldsymbol{k_i}| = \sqrt{2mE_i}/\hbar$). After interaction with the sample, a fraction of the incident beam is scattered into a small solid angle $d\Omega$ (the angles 2θ and Φ define the direction of the scattered beam), with final wavevector $\boldsymbol{k_f}$ and energy E_f. $\boldsymbol{q}$ is the corresponding wave vector transfer. The number of scattered neutrons may be monitored by a detector at a distance *r* that covers this range of solid angle.

The above mentioned cross-section is given by Fermi's Golden rule,

$$\frac{\partial^2\sigma}{\partial\omega\partial\Omega} = \left(\frac{m_n}{2\pi\hbar^2}\right)^2 \frac{k_f}{k_i} \sum_{v,v'} p_v \left|\langle v'|\hat{V}|v\rangle\right|^2 \delta(\hbar\omega + E_v - E_{v'})$$

where v and v' are initial and final states of the scatterer with corresponding energies E_v and E_v', m_n is the neutron mass, k_i and k_f are initial and final neutron wave numbers, and p_v is the population factor of the initial states. The interaction potential $\hat{V}$ is the sum of two parts: one arising from nuclear interaction with the nuclei

$$\hat{V}_{\text{nucl}} = \frac{2\pi\hbar^2}{m_n}\sum_i b_i\delta(\mathbf{r}-\mathbf{r}_i)$$

which we are not interested in here, and a second arising from the interaction with the magnetic field $\boldsymbol{B}$ in the sample

$$\hat{V}_{\text{magn}} = -\gamma\hbar\,\hat{\mathbf{s}}\cdot\mathbf{B}$$

where $\hat{s}$ is the operator of the neutron spin and $\gamma/2\pi = -2916.4$ Hz/G is the gyromagnetic ratio of the neutron. The matrix elements can be evaluated (Lovesey, 1984; Williams, 1988) and with some assumptions (unpolarized beam, no orbital moments contribute to $\boldsymbol{B}$) one arrives at

$$\frac{\partial^2\sigma}{\partial\omega\partial\Omega} = (\gamma r_0)^2 \frac{k_f}{k_i} |F(\mathbf{q})|^2 e^{-2W(\mathbf{q})} \sum_{\alpha\beta}\left(\delta_{\alpha\beta} - \frac{q_\alpha q_\beta}{q^2}\right) S^{\alpha\beta}(\mathbf{q},\omega)$$

(the case of scattering from orbital moments is more complicated). This expression contains the momentum transfer $\mathbf{q}$, the classical electron radius $r_0 = 0.282\times10^{-12}$ cm, the magnetic form factor $F(\mathbf{q})$ (see below), the Debye-Waller factor $e^{-2W(q)}$, and the magnetic scattering function

$$S^{\alpha\beta}(\mathbf{q},\omega) = \frac{1}{2\pi\hbar}\int_{-\infty}^{\infty} e^{-i\omega t}dt \sum_{ij} e^{i\mathbf{q}(\mathbf{r}_i - \mathbf{r}_j)}\langle\hat{S}_i^\alpha(0)\hat{S}_j^\beta(t)\rangle$$

where $\hat{S}_i^\alpha$ ($\alpha = x,y,z$) is the spin operator of the ion at site $\mathbf{r}_i$ and brackets mean the thermal average. Some important features can be read from these formulae. First, and most important, the factor

$$\left(\delta_{\alpha\beta} - \frac{q_\alpha q_\beta}{q^2}\right)$$

implies that only components of the magnetic moment density perpendicular to $\mathbf{q}$ are relevant in magnetic scattering. Second, the form factor $F(\mathbf{q})$, which is the Fourier transform of the spin density associated with the magnetic moment, is monotonically falling off with $\mathbf{q}$ and suppresses magnetic scattering intensity towards high $\mathbf{q}$. Form factors can be measured using polarized neutrons (Brown et al., 1999) or calculated (Desclaux and Freeman, 1984) and can be found in tables (Brown, 1992). Last but not least, $S^{\alpha\beta}(\mathbf{q},\omega)$ is the Fourier transform in space and time of a pair correlation function giving the probability that if the magnetic moment at site $\mathbf{r}_i$ has some vector value at time 0, then the moment at site $\mathbf{r}_j$ has some other value at time t.

A similar interpretation of the scattering cross-section in terms of correlation functions is also valid for nuclear scattering.

3. 1. 2 Polarized Neutron Beam Instrumentation

This chapter describes the basic means used to polarize a neutron beam and to handle the polarization. A neutron beam is said to be polarized if the beam average of the individual magnetic moments of the neutrons is non-zero. The beam polarization P can be determined by measuring the numbers of spin "up" (N_{up}) and spin "down" (N_{down}) neutrons in the beam:

$$P = \frac{N_{up} - N_{down}}{N_{up} + N_{down}}$$

The common methods to polarize neutrons are:
  (1) Transmission or reflection from magnetic mirrors or supermirrors;
  (2) Bragg diffraction from a magnetic crystal;
  (3) Transmission through a polarized ^{3}He filter.

We shall describe these methods briefly. More detailed reviews can be found in the literature (Williams, 1988; Cussen et al., 2000; Anderson et al., 2000). Let us note here that neutron sources of the next generation (like the SNS under construction at Oak Ridge National Laboratory) will produce pulsed beams. Here neutrons are effectively monochromatized by their time-of-flight between moderator, sample, and detector because the velocity is inversely proportional to the wavelength. Monochromators are therefore much less used for instruments at a spallation source. Instruments at pulsed sources that make use of monochromators are mostly spectrometers for inelastic scattering, where crystals are used either to define the incident or to analyze the final energy of the neutron. However, ^{3}He spin filters are well suited for pulsed beams and also supermirror-based polarizers can be designed to handle broad bandwidth neutron beams (Krist et al., 1998).

Magnetic mirror polarizers use total reflection of neutrons from magnetic surfaces or thin films (see Fig. 3. 3). The refractive index of a magnetized material contains two parts, one due to the nuclear scattering length density and one due to the magnetic. The latter is proportional to the magnetization **M** and depends on the orientation of the neutron spin with respect to the vector **M**. Hence it is different for up (+) and down (-) neutrons. The critical angle for total reflection of neutrons from a magnetic surface is

$$\theta_C^\pm = \lambda \sqrt{\frac{n}{\pi}(b \pm p)}$$

where λ is the neutron wavelength, n the number of atoms per unit volume, and b and p are the average coherent nuclear and magnetic scattering length, respectively. Thus, for a neutron beam that strikes the surface within the angular range between θ_c^- and θ_c^+ (note that these angles depend on the neutron wavelength), the reflected beam will practically consist only of spin-up neutrons and therefore be highly polarized. By alloying, one can match b and p such that one spin state (in most cases spin-down) is not reflected at all and thus create a polarized reflected beam for an incident angular range between 0° and θ_c^+. In the case that a neutron-transparent substrate is used, one can also use the transmitted beam since it is polarized as well (see Fig. 3. 3). Such a device is effectively a "spin splitter" (Krist et al., 1998; Lee and Majkrzak, 1999). Unfortunately, typical values for b and p are very small such that polarizers based on single magnetic layers - even for large neutron wavelengths of several Å - only allow an angular coverage of a few mrad.

A large improvement was made by artificially increasing the critical angle by using multilayer Bragg reflections from a "supermirror" structure (Mezei and Dagleish, 1977). A typical polarizing supermirror consists of a magnetic / non-magnetic layer sequence, in which for spin-down neutrons the scattering length density (SLD) of the magnetic layer matches exactly the SLD of the non-magnetic layer [a possible combination is $Fe_{89}Co_{11}$ as the magnetic and Si as the non-magnetic material (Krist et al., 1988)]. If this is the case, then spin-down neutrons do not experience any contrast (or potential difference) at the interfaces of these materials and are, consequently, not reflected by the

multilayer structure. In contrast, spin-up neutrons experience a strong contrast between the layers such that they are strongly reflected. A supermirror layer sequence does not consist of only one single multilayer period since this would only reflect a particular wavelength/angle of incidence combination. Instead, the multilayer period is slowly varied throughout the layering sequence. This allows handling of a larger range of wavelength/angle combinations.

Nevertheless, there is a natural limitation of the method that can be seen in the formula: even for state-of-the-art supermirrors, for thermal neutrons θ_C is still in the mrad range (for polarizing coatings, up to three times the critical angle of natural Ni has been achieved), therefore they work best for cold neutrons, but the accepted angular range is always relatively small. Modern mirrors reach typical beam polarizations of 95%-98% at a spin "up" neutron reflectivity of about 90%. In transmission geometry, the spin "down" neutron throughput is reduced to about 80% due to absorption effects.
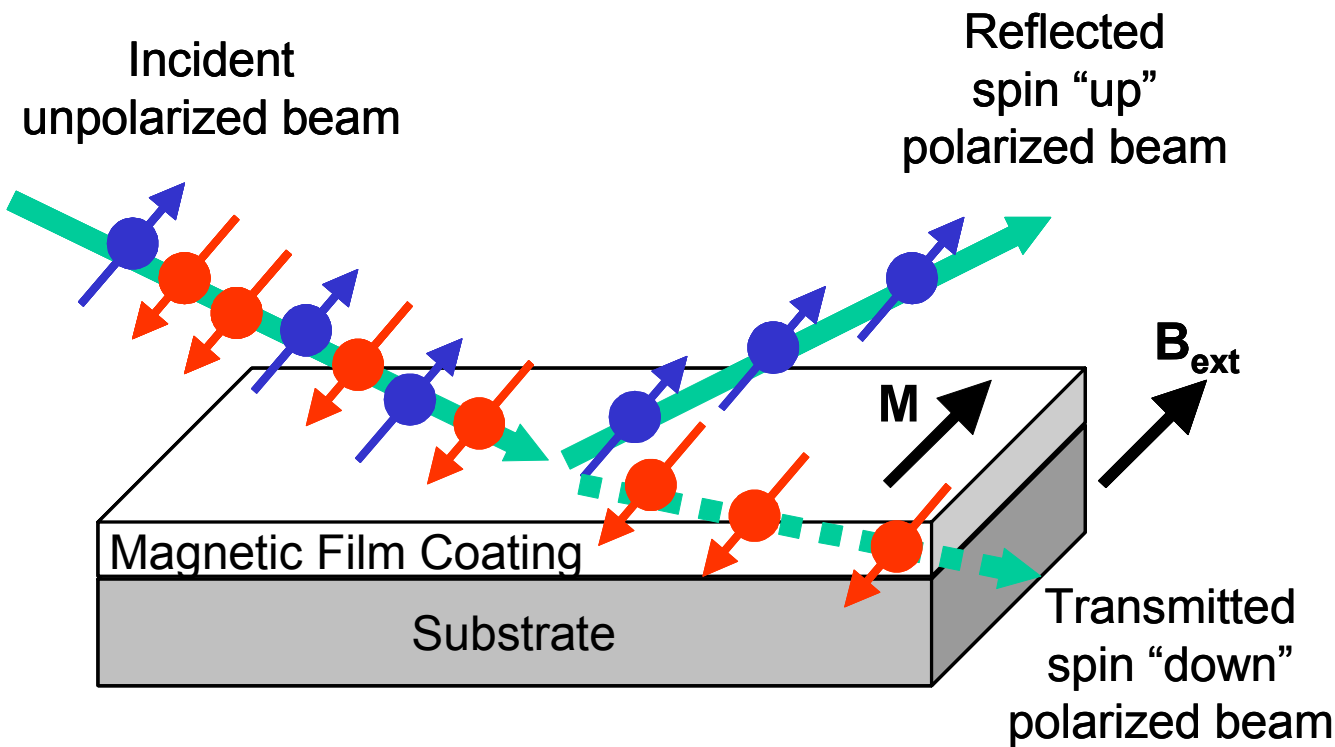

Figure 3. 3   Magnetic thin film polarizer. The external magnetic field ("guide field") B_{ext} defines the spin eigenstate. It is desired that only non-spin flip scattering takes place. Therefore, the sample magnetization should only have components that are collinear with the incident neutron polarization. Hence, B_{ext} must be strong enough to fully saturate the film magnetization M. [An exception is a "remanent" polarizer (Boeni et al., 1999). In this case, M is antiparallel to B_{ext} resulting in reflection of spin "down" neutrons.]

The (111) reflection from the ferromagnetic Heusler alloy Cu_2MnAl (Freund et al., 1983) can be used to polarize cold and thermal neutrons. This is convenient for instruments that use a monochromatic beam (for example, diffractometers and triple-axis spectrometers at reactor installations) because polarization and monochromatization are done simultaneously. If the crystal is placed in a vertical field, the magnetic moments are aligned along the field direction and the magnetic scattering is entirely non-spin-flip. The structure

factor of the (111) reflection gives scattered intensities "up" and "down" of

$$I^+ \propto (b_{Al} - b_{Mn} + p_{Mn})^2$$ and $$I^- \propto (b_{Al} - b_{Mn} - p_{Mn})^2$$, respectively, where the b's are the nuclear scattering lengths of the elements and p_{Mn} is the magnetic scattering length. The particular property of this alloy is that $b_{Al} - b_{Mn} \cong p_{Mn}$, so the spin-down intensity is small and a polarization of 95% can be routinely achieved. The drawback is that the reflected intensity is still much smaller than for a pyrolytic graphite monochromator (the loss factors are about 5 at 2.4 Å and about 10 at 1.5 Å), mainly because of the smaller mosaic spread of the available crystals.

For cold neutron instruments it is, in the majority of cases, better to polarize with a supermirror and monochromatize independently using a pyrolytic graphite crystal (unless Heusler crystals with sufficiently large mosaicity are available). This approach has the additional advantage that, due to the low neutron absorption of graphite, the spectrum transmitted by the monochromator can be used to feed neutrons to other instruments downstream the neutron guide. The decoupling of monochromatization and polarization can be an advantage for triple-axis spectrometers since it allows for a more flexible resolution setting.

Polarizing filters based on preferential scattering or absorption of one of the neutron spin states have been known for decades (Williams, 1988). Various techniques have been developed but none of them have become widely accepted for various reasons (insufficient polarizing efficiency, unfavorable neutron energy-dependence, low transmittance, too complicated setup, high cost etc.). A more recent and very promising development, however, is the helium spin filter. Although it has been recognized since the 1960s that polarized ^{3}He gas might be an extremely useful spin filter for thermal and epithermal neutron beams (Passell and Schermer, 1966), the feasibility could be demonstrated only recently (Coulter et al., 1990). The device is based on the spin-dependence of the neutron absorption by the ^{3}He isotope. At neutron energies typically used in neutron scattering, absorption is largely dominated by the reaction $^3\text{He}^\uparrow + n^\downarrow => {}^4\text{He}^* => {}^1\text{H} + {}^3\text{H}$, which goes entirely through the singlet state of the compound nucleus with zero spin, that is, only the neutron spin state with spin antiparallel to the ^{3}He spin contributes to the absorption cross-section for capture of neutrons. At a neutron energy of 25 meV, the cross-section is 10666 barns for neutrons with spin antiparallel to the ^{3}He nuclear spin, while the total cross-section for absorption or scattering of neutrons with parallel spin is only a few barns (Mughabghab et al., 1981). This makes it possible to construct a spin filter device provided the ^{3}He can be polarized. For a sufficient column density (atomic density $\times$ length of the cell) of 100% polarized ^{3}He, the transmission of neutrons with parallel spin would approach 100%. This transmitted neutron beam would be 100% polarized since virtually no neutrons with antiparallel spin could pass through the cell.

Highly polarized ^{3}He can be obtained by two methods that use optical pumping techniques: spin exchange with optically pumped Rb, and metastability exchange optical pumping in ^{3}He. In recent years, both

approaches have been used successfully in polarization and analysis experiments of neutron beams (Heil et al., 1999; Cussen et al., 2000; Rich et al. 2001; and references therein).

^{3}He spin filters show many favorable characteristics: ① they are appropriate for polarizing/analyzing neutrons of a very broad energy range from cold to epithermal, ② they are suitable for broad wavelength band experiments, ③ their beam polarization is highly homogeneous, ④ they have a predictable transmission function, ⑤ a large solid angle of detection is possible, and ⑥ their additional contribution to the beam divergence is minimal. Due to these features, the main application of ^{3}He is polarization analysis in experiments that require large angular coverage, e.g. small-angle scattering, diffuse scattering, off-specular neutron reflectometry etc. For these applications, the use of ^{3}He is a good alternative compared to a complicated and expensive arrangement of supermirrors to cover large solid angles (although, once installed, the latter do not require further maintenance). In contrast, supermirrors are usually superior in experiments that require only small angular coverage at lower neutron energies, e.g. specular reflectometry.

^{3}He spin filters are, however, not yet fully mature devices. Issues that require further technical development include: ① improving the ^{3}He polarization reliably beyond the current experimental limit (in state-of-the-art cells, polarization values in the range of 70%-80% have been achieved), ② achieving reproducible and very long relaxation times, ③ fabricating large solid angle cells, and ④ shielding the cell from magnetic field gradients resulting from high sample fields. The first point is of particular importance. Due to the non-perfect ^{3}He polarization, the "wrong" neutron polarization state (antiparallel) is partially transmitted, whereas the desired parallel neutron spin state is partially absorbed. Therefore, in order to achieve high neutron beam polarization, a relatively large column density of ^{3}He gas is required, which implies low transmission. A state-of-the-art ^{3}He cell designed for achieving a neutron beam polarization of 95%, a typical value for a polarizing supermirror, will provide approximately three times less neutron flux than a supermirror polarizer. Another problem related to the non-perfect polarization of the ^{3}He gas is that neutron polarization power and transmission are coupled and neutron-wavelength dependent. For experiments that require using broad neutron bandwidth, optimum conditions (in terms of achieving a particular set of values for neutron polarization and transmission) can be achieved only for a limited range of wavelengths.

We now turn our attention to the behavior of the neutron spin in a magnetic field. To manipulate the neutron spins of a polarized beam, a magnetic field is needed, and for a general discussion the time evolution of an individual spin in such a field can be classically described by the well-known Larmor equation,

$$\frac{d}{dt}s(t) = \gamma[s(t) \times B(t)]$$

where $\gamma/2\pi$ = -2916.4 Hz/G is the gyromagnetic ratio of the neutron, **B** is the magnetic field, and **s** is the spin vector of the neutron. **B**(t) refers to the time evolution of the magnetic field that the neutron experiences along its trajectory, i.e. in the stationary frame of the moving neutron. Remembering that the neutron is a spin 1/2 particle, and conventionally taking the direction of the **B** vector as the **z** axis, the two most important solutions of this equation are:

(1) **s**(t=0)||**B**, in this case the operator of the spin is in a **z** eigenstate and hence $s(t)$ is constant. Simple polarization analysis basically uses this case (with the exception of a necessary spin flipper device).

(2) **s**(t=0)⊥**B**, in this case $s(t)$ is not constant, and the beating between x and y states results in what is classically understood as Larmor precession of the spin. The most prominent instrumental application of Larmor precession of a neutron beam is neutron spin echo (see Section 3. 3. 2).

Case (1) means that the polarization, once "prepared" to be parallel to the field direction, will stay parallel to the field (hence the term guide field for **B**), as long as the direction of the B-field does not change. If the field direction does change, say, in the frame of the moving neutron with a typical frequency ω, two cases have to be considered that relate ω to ω_L = γB, the Larmor frequency defined by the modulus of the field:

(1) $\omega \ll \omega_L$ (slow or "adiabatic" field change), as for example in a field that is spatially changing direction slowly along the neutron trajectory. The neutron spin follows the field rotation adiabatically and essentially stays parallel to the local field direction.

(2) $\omega \gg \omega_L$ (sudden or "non-adiabatic" field change), as for example if the neutron beam passes through a thin metal foil that carries a dc current (the magnetic field vectors before and behind the current sheet point in opposite directions). In cases when there is a non-zero angle between the direction of the neutron spin and the new B-field vector, the neutron spin starts precessing around this new local field direction. This is made use of in spin flipper devices.

Technically, guide fields of a few Gauss are sufficient to prevent the earth field or stray fields from neighboring installations from disturbing the local field direction.

Besides a magnetic guide field that is necessary to keep the polarization, other devices are often needed which turn the polarization direction with respect to the guide field direction. Generally, this is achieved by making use of non-adiabatic (sudden) changes of the field direction which the neutron spin can not follow. Different types of these "spin flippers" are in use. A simple
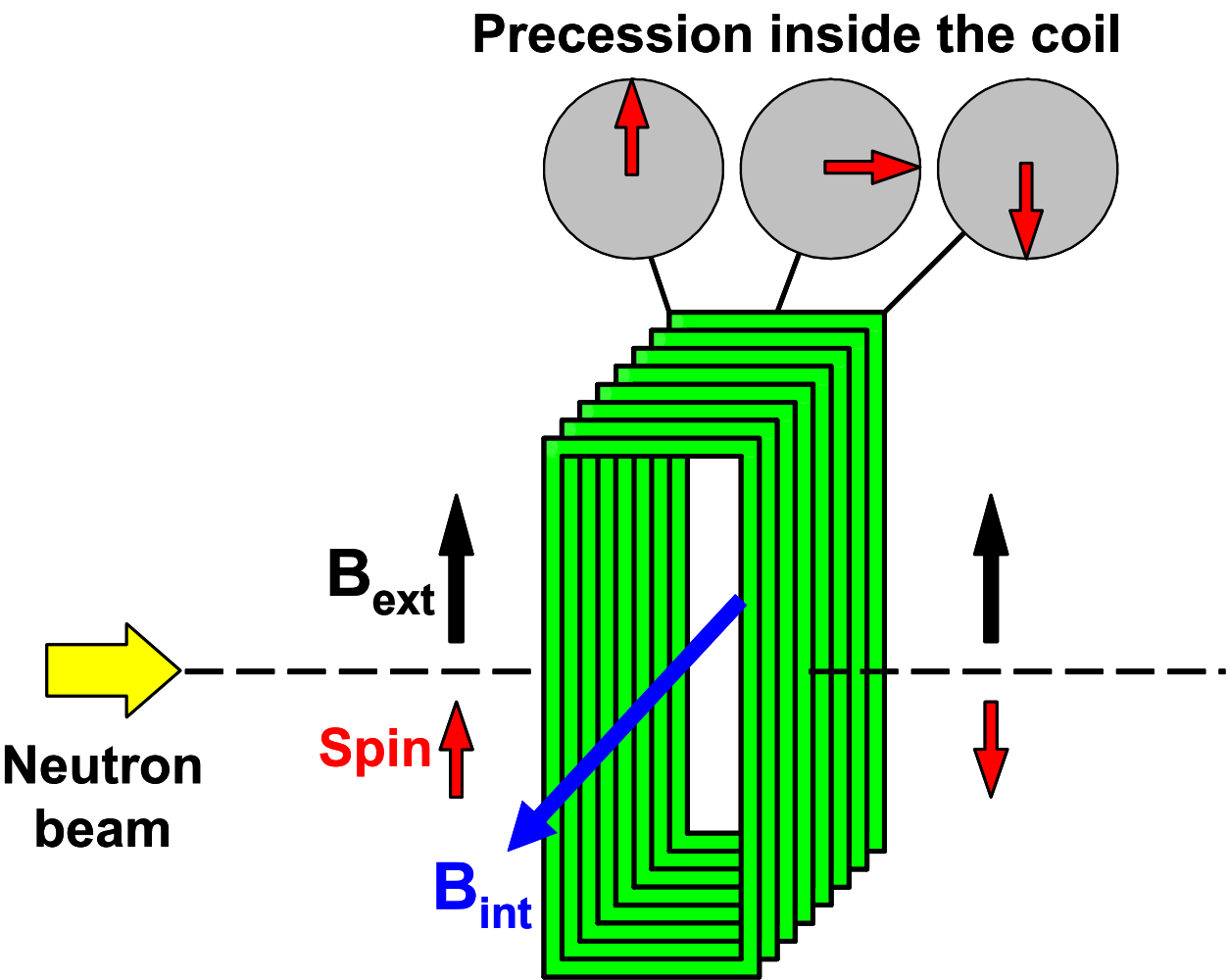
Precession inside the coil

Figure 3. 4   Schematic diagram of a Mezei-type spin flipper. B_{int} is chosen such that the polarization is inverted, i.e. turned by π, when the neutron exits the flipper. An additional coil, which is needed to cancel the guide field B_{ext} within the flip-field region, has been omitted for clarity. The windings of this coil would be perpendicular to the windings of the flip field coil that is shown, creating an extra field that is perpendicular to B_{ext}.

example is the Mezei flipper, which is basically a flat coil placed in the beam which creates a field highly localized in its interior. This flipping field B_{int} is perpendicular to the external guide field B_{ext} (see Fig. 3. 4). It is important to note that in this design the external guide field is cancelled within the flip field region by a second coil placed around the flipper coil. When the neutron enters the flipper, it experiences a sudden change of the field direction, such that the spin precesses around the inner flipper field while the neutron is passing through the coil (Larmor precession). The magnitude of this field may be tuned to turn the neutron spin, for example, by π so that the neutron polarization is inverted with respect to the guide field direction when the neutron exits the flipper. An extensive review about different types of flippers, for example radiofrequency flippers, cryo flippers etc., may be found in (Williams, 1988).

3. 1. 3 The Polarization of the Scattered Beam

For the characterization of magnetic materials the analysis of the polarization of the scattered beam is an essential part of the scattering experiment (Shull

et al., 1951b). If the beam incident on the sample is polarized, performing this analysis allows one to separate nuclear and magnetic scattering. We now elaborate on this point a bit further.

The nuclear scattering potential $\hat{V}_{nucl}$ (see above) sums the individual b's, which for nuclei with spin can be written as (Lovesey, 1984):

$$\hat{b} = A + \frac{1}{2}B\hat{s}\cdot\hat{i}$$

where A and B are isotope-specific numbers, and $\hat{s}$ and $\hat{i}$ are the spin operators of neutron and nucleus, respectively. The spin-independent part of the potential gives rise to scattering without spin-flip, because the neutron spin is not involved (usually referred to as coherent nuclear scattering). If the sample contains isotopes with different scattering lengths, local fluctuations around the mean value of A give rise to isotope-incoherent scattering (also without spin flip). The $\hat{s}\cdot\hat{i}$ term tells that, if the nucleus has a spin, two different compound nuclear states with total spins (i+1/2) and (i-1/2) may be formed during scattering, with probabilities (i+1)/(2i+1) and i/(2i+1), and in general their scattering lengths will be different. As for different isotopes, this creates incoherent scattering, but this time a spin-flip is involved. Generally, scattering from a magnetic moment μ or a nuclear magnetic moment i is without spin-flip for the component of μ or i parallel to $\hat{s}$, whereas the two components perpendicular to $\hat{s}$ will scatter with spin-flip (Moon et al., 1969). Usually nuclear spins are not ordered and this contribution to the scattering (hence called spin-incoherent scattering) is then 2/3 with spin-flip and 1/3 without spin-flip. At extremely low temperatures ordered nuclear moments may give rise to magnetic scattering effects.

Given an initial beam polarization **P**, we may summarize the effect of the different types of scattering on the scattered beam polarization **P'** as follows:

Nuclear scattering (coherent or isotope-incoherent): **P' = P**

Spin-incoherent scattering: **P' = -1/3 P**

Magnetic scattering from macroscopically isotropic magnetic systems (usually from unpaired electrons; at extremely low temperature also from nuclear magnetic moments):

$$\mathbf{P'} = -\frac{\mathbf{q}(\mathbf{q}\cdot\mathbf{P})}{q^2}$$

The last formula was first obtained by Halpern and Johnson in their classic paper on magnetic neutron scattering (Halpern and Johnson, 1939). Its meaning is: The scattered beam is polarized in the direction of the scattering vector **q**, the spin is flipped, and the polarization also depends on the relative orientation of **q** and **P**. The formula is not universal, however, it holds only for macroscopically isotropic cases, for example paramagnets, collinear antiferromagnets, generally powder samples, and (non-magnetized) multidomain ferromagnets (as long as they do not depolarize the beam), but not for macroscopic single crystals with non-collinear magnetic order.

Figure 3. 5 shows a classical example of how paramagnetic moments can be measured (Moon et al., 1969). The substance used was a MnF_2 powder. The unpolarized beam data set (upper panel) shows Bragg peaks at various scattering angles together with a distinct background signal that falls off towards high q. In the polarized beam measurements (**P** was kept parallel to **q**), the Bragg peaks appear only in the non-spin-flip channel (middle). This clearly verifies their non-magnetic origin. The spin-flip channel contains solely the paramagnetic scattering signal (lower panel), decaying corresponding to the characteristic form factor of the Mn^{2+} ion.

In the most general case, when the Halpern/Johnson formula can not be used, we have to write

$$\boldsymbol{P}' = \hat{\boldsymbol{S}}\boldsymbol{P} + \boldsymbol{P}''$$

where $\hat{\boldsymbol{S}}$ is called the polarization tensor and $\boldsymbol{P}''$ is the polarization created by the scattering process. $\hat{\boldsymbol{S}}$ has (at most) six independent elements. These can be measured if the magnetic sample is kept in zero external magnetic field. The corresponding technique is called spherical polarization analysis (Brown et al., 2002; see also Section 2. 2 for a detailed description of the D3 instrument and the CRYOPAD device). The required formulae for the individual elements of $\hat{\boldsymbol{S}}$ and $\boldsymbol{P}''$ can be found in the literature in a handy form (Brown, 2001). Since the experimental setup is difficult, and the diagonal elements of $\hat{\boldsymbol{S}}$ can be measured in an easier way (see below), the technique is only applied if $\hat{\boldsymbol{S}}$ has off-diagonal elements. Such elements may appear in magnetic crystals with non-collinear magnetic order (for example, canted or helical structures), magneto-electric crystals (for reference and examples, see Brown, 2001). If they do, spherical polarization analysis is the only way today to access them experimentally.

Using a magnetic guide field at the sample position in order to keep the neutron beam polarization is experimentally easier to realize and allows one to measure the three diagonal terms of $\hat{\boldsymbol{S}}$. This technique is called three-directional polarization analysis (Schärpf and Capellmann, 1993). More technical details will be discussed together with the D7 instrument in Section 2. 2. Nuclear and spin-incoherent neutron scattering always appear in the diagonal elements of $\hat{\boldsymbol{S}}$, because $\boldsymbol{P}$ and $\boldsymbol{P}'$ are parallel. The same holds for magnetic scattering, if the Halpern/Johnson formula can be applied. Thus, in many cases, the three diagonal terms of $\hat{\boldsymbol{S}}$ contain all information about the sample one wants to obtain in a neutron scattering experiment.
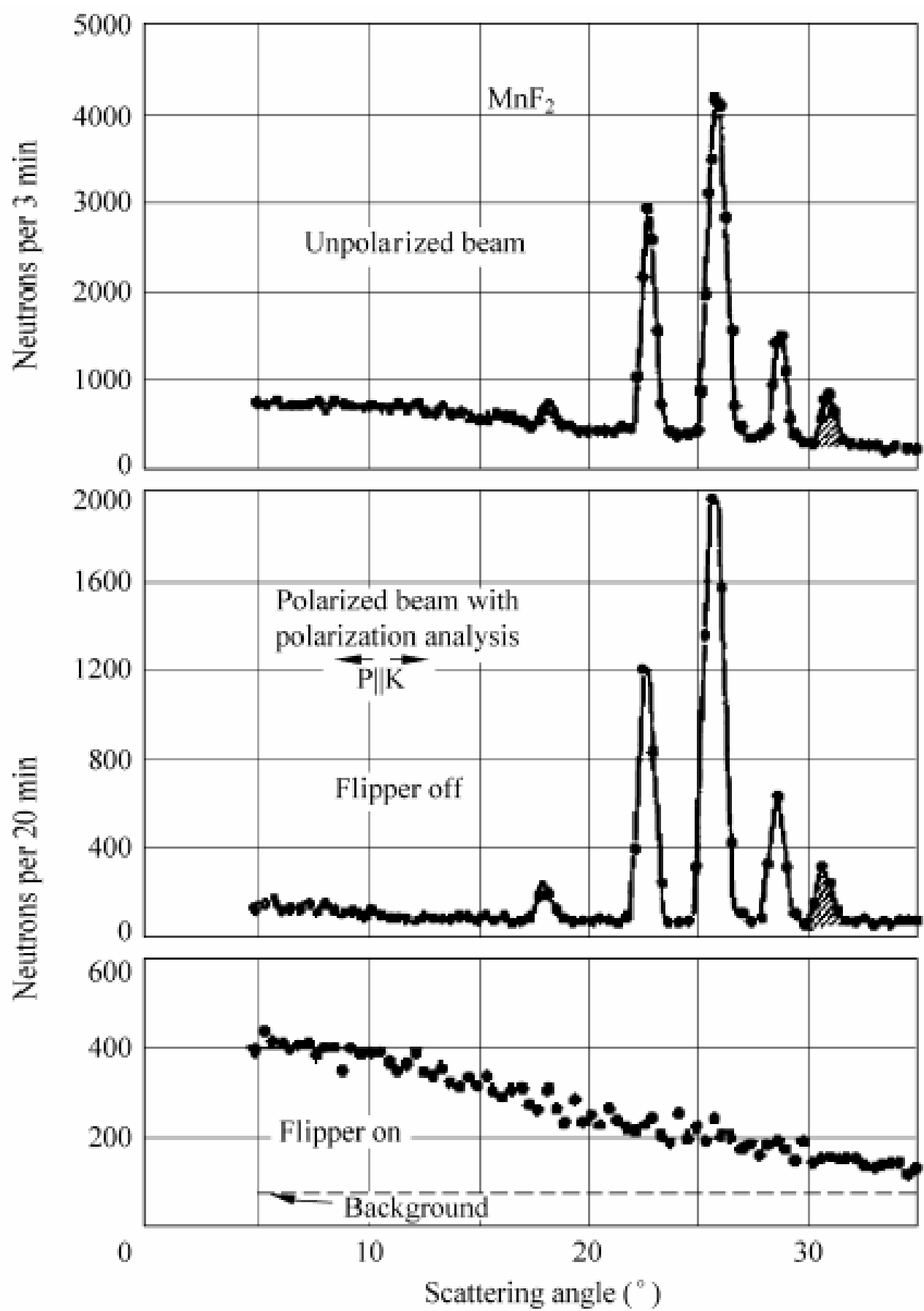
Figure 3. 5   Separation of paramagnetic scattering through polarization analysis. Upper panel: unpolarized beam measurement; middle: polarized beam measurement (non-spin-flip channel); lower panel: spin-flip channel. Note that the polarized beam data have much lower absolute count rates compared to the unpolarized beam measurement because of intensity losses associated with the polarizer/analyzer equipment (Moon et al., 1969).

3. 2   Elastic Magnetic Scattering

3. 2. 1 Small-Angle Scattering

Small-angle neutron scattering (SANS) is extensively used for investigating nanostructured materials. It probes length scales in the nanometer regime and thus can be used to study microstructural features of matter such as size, shape and magnetization of precipitates. As in other diffraction experiments, the SANS intensity is measured as a function of the momentum (more precisely wave vector) that is transferred from neutron to sample during the scattering process, i.e. as a function of the scattering vector $\boldsymbol{q}$:

$$\boldsymbol{q} = \boldsymbol{k}_i - \boldsymbol{k}_f$$

The scattering vector $\boldsymbol{q}$ is simply the difference between the neutron's incident wave vector $\boldsymbol{k}_i$ and its scattered wave vector $\boldsymbol{k}_f$. In SANS experiments, the scattering is assumed to be elastic, i.e. $|\boldsymbol{k}_i| = |\boldsymbol{k}_f| = 2\pi/\lambda$ and $|\boldsymbol{q}| = 4\pi \sin(\theta)/\lambda$, where λ is the neutron's wavelength and 2θ is the scattering angle. The momentum transfer is inversely proportional to the length scale of investigation. The available q range of SANS instruments is between 10^{-1} Å^{-1} and 10^{-4} Å^{-1} corresponding to mesoscopic object sizes in the range between approximately 10 Å to 10000 Å. In contrast, in the diffraction regime, q is on the order of 1 Å^{-1} and therefore suitable for probing interatomic distances.

The intensity is obtained by summing up the scattering amplitudes of all atoms in the sample, weighted by the phase shift at each atomic position $\boldsymbol{r}$:

$$I(\mathbf{q}) = \left| \int b(\mathbf{r}) e^{i\mathbf{q}\cdot\mathbf{r}} d^3 r \right|^2 ,$$

where the integral extends over the entire sample and $b(\mathbf{r})$ is the local (coherent) scattering length density. For magnetic materials, the latter has magnetic contributions. As discussed in Section 3. 1, not only the magnitude of the local magnetic moment but also its orientation relative to the incoming neutron polarization play a role in the scattering process.

Small-angle scattering signals resulting from the magnetic microstructure can be separated from those resulting from variations in the atomic density or secondary phases. For unpolarized neutron beam experiments, this can be done by investigating the magnetic field dependence of the SANS signal. Using polarized neutrons, one can extract magnetic information by variation of the incident neutron beam polarization in a fixed external field (Wiedenmann, 2001).

The following is an excellent example of the usefulness of SANS measurements using unpolarized neutron beams. Weissmueller et al. recently investigated the magnetic properties of nanocrystalline Co and Ni samples and demonstrated that SANS measurements are able to provide quantitative information on ① the magnetic microstructure, ② the exchange stiffness constant, and ③ the magnitude and microstructure of the magnetic anisotropy of these materials (Weissmueller et al., 2001).

Nanocrystalline ferromagnets have interesting magnetic properties due to their strongly reduced grain size d. As the latter reaches nanometer dimensions, random jumps in the local orientation of the magnetic easy axis are introduced, leading to altered magnetic properties compared to ordinary polycrystalline bulk materials.   The effect of the reduced grain size on the magnetic properties critically depends on the magnitude of the grain size relative to a magnetic exchange length $l_K = \sqrt{A/K}$, where A is the ferromagnetic exchange-stiffness constant, and K an anisotropy energy coefficient. Nanocrystalline hard magnets have $l_K < d$, with the magnetization axis locked onto the easy axis of each grain and an enhanced remanence due to gradients in the orientation of the magnetization at grain boundaries. By contrast, nanocrystalline soft magnets have $l_K > d$. In this case the magnetization cannot follow the changes in the orientation of the easy axes on the scale of the grain size. Instead, the local magnetization direction results from an effective averaging of the anisotropy in many neighboring grains. As the work of Weissmueller et al. demonstrates, SANS is an excellent tool for measuring magnetic structures in these length scales.

The nanocrystalline Co samples that are the subject of the following discussion were prepared by pulsed electrodeposition. Although the mass density was practically identical with that of bulk Co, the structural grain size was found to be quite small, about 10 nm, and the mean distance between stacking faults was even smaller, only about 2 nm. Since the volume fraction of structural inhomogeneities is small, the ratio of magnetic scattering signals to the magnetism-independent nuclear scattering backgrounds in the SANS data were relatively high, allowing this effect to be observed.
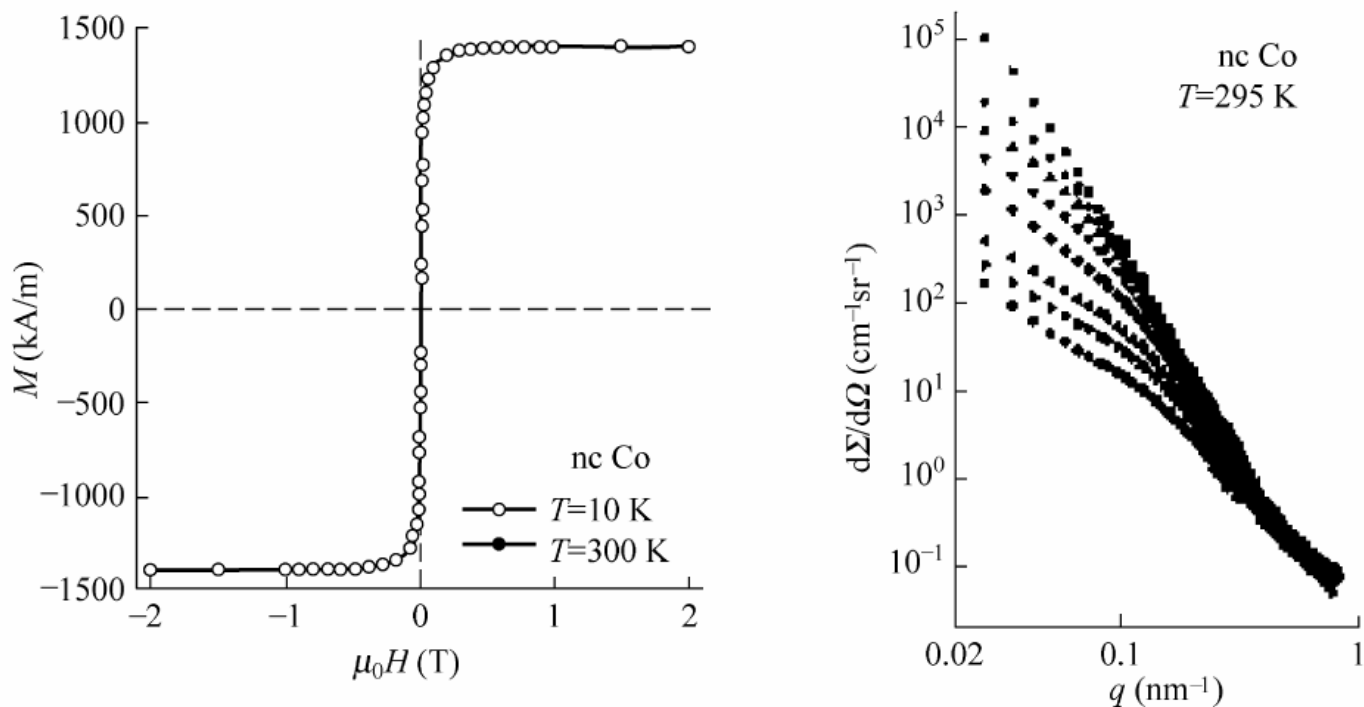

Figure 3. 6   (a) Magnetization isotherms at T = 10 K and 300 K for nanocrystalline Co. (b) Experimental differential scattering cross-section $d\Sigma/d\Omega$ versus modulus q of the scattering vector for magnetic fields of (from top to bottom) 5, 43, 87, 180, 390, 770, 1140, and 1740 mT (Weissmueller et al., 2001)

Figure 3. 6 compares magnetization and magnetic SANS data of the nanocrystalline Co sample. The hysteresis loop measurements (see Fig. 3. 6 a) indicate that the material apparently saturates in fields of about 0.5 T. The magnetization data are practically identical for low-temperature (10 K) and ambient temperature measurements. Figure 3. 6b shows that SANS measurements, which in this case essentially probe the spatial homogeneity of the magnetic moment orientations, reveal complementary information: In contrast to the seemingly saturated magnetization, there are still substantial changes in the SANS signal as the magnetic field is increased beyond 0.5 T. Due to this strong field-dependence it can be excluded that the scattering originates from magnetized particles in a non-magnetic matrix or from non-magnetic particles or pores in a magnetic matrix. The scattering contrast between a particle and the matrix would remain essentially constant, independent of H, once the sample was near saturation. Therefore, the authors argue that the scattering must result from a continuous, small, and periodic variation of the spin-misalignment angle relative to the overall direction of the field. This hypothesis is supported by the fact that the curvature in the log-log plots of differential scattering cross-section $d\Sigma/d\Omega$ versus q is shifted to larger q as the field strength is increased. In SANS data the scattering vector at maximum curvature often corresponds to 2π over a characteristic length scale; therefore, the observation is consistent with the notion that increasing the magnetic field leads to a suppression of the long-wavelength magnetic fluctuations of the magnetization, so that the dominant wavelength is progressively reduced.

Another important result of these SANS measurements is that other factors besides the grain size d can significantly affect the magnetic microstructure. Examples of such factors are twin boundaries and centers of strong anisotropy or of antiferromagnetic coupling, potentially due to changes in the atomic coordination and interatomic spacing in the core of grain boundaries or dislocations.

In general, magnetization distributions can be studied with unpolarized neutron beams (i.e. with randomly oriented spins) if the scattering intensities from chemical and magnetic structures are of the same order of magnitude. The utilization of polarized neutrons has one major advantage: it makes it possible to modify the relative contrast between magnetic and non-magnetic particles, amplifying weak magnetic signals that may be shadowed by strong scattering from other sources (for example nuclear scattering due to finite grain size). Polarized SANS does not necessarily need to include polarization analysis of the scattered neutrons, although this can be done for example by using a ^{3}He filter system (see Section 3. 1. 2). In certain situations, polarization analysis reveals further details regarding the relative orientations of the magnetic domains in the sample.

Because of experimental difficulties and a strong reduction in neutron flux that is inherent to polarized beam techniques, only a few of the ≈ 25 SANS instruments in the world have a polarized beam option available. As an example, Figure 3. 7 shows the schematic layout of the polarized neutron SANS instrument at Hahn-Meitner Institute Berlin (Keller et al., 2000).
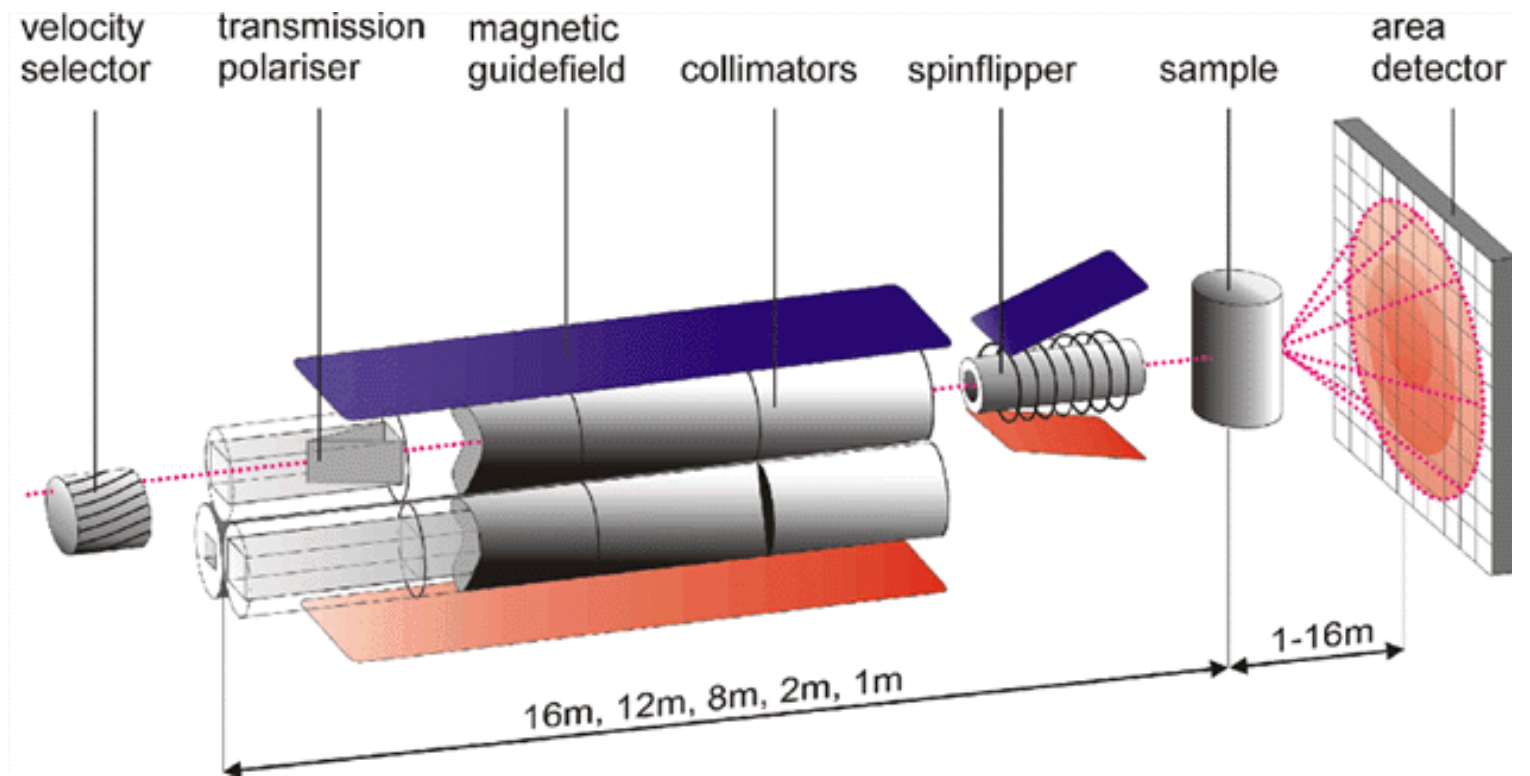
Figure 3. 7   Polarized SANS instrument V4 at Hahn-Meitner Institute Berlin (figure taken from HMI web site).

Neutrons enter from the left and are monochromatized ($\Delta\lambda/\lambda \approx 10\%$) using a velocity selector. Beam polarization is achieved by using a wedge-shaped supermirror transmission polarizer which can be rotated into the beam. This kind of polarizer has a distinct advantage, particularly for SANS applications: since it uses only the transmitted neutrons, it does not deflect the beam and therefore does not require a realignment of the 30 m long instrument. The polarizer is installed in the first section of the 16 m long collimator drum. The collimation length is variable (minimum: 1 m, maximum: 12 m) in order to achieve variable angular resolution. Collimation sections that are not in use are replaced by Ni neutron guide sections via a drum mechanism. The beam size and collimator aperture openings are 3 cm $\times$ 5 cm. A magnetic guide field of about 10 G is needed between the polarizer and the sample to avoid depolarization of the neutron beam. A radio-frequency spin flipper, consisting of a longitudinal ac magnet field coil and a static gradient magnet field, is installed in front of the sample to allow measurements with both neutron polarizations. A particular feature of this spin flipper design is that no material is needed in the path of the beam. This is important for high-resolution SANS applications because small-angle scattering from the wire materials that are used in the usual Mezei flipper design (see Fig. 3. 7) would seriously degrade the angular resolution of the instrument. In order to cover different q ranges, the two-dimensional ^{3}He-detector with 64 $\times$ 64 elements of 1 $\times$ 1 cm^2 can be positioned at any distance between 1 and 16 m from the sample in the horizontal direction. In the polarized neutron mode, the V4 instrument achieves > 30% of the corresponding unpolarized neutron flux at shorter wavelength ($\lambda \approx 6$ Å) decreasing to 10% at higher wavelength. The values for the beam polarizations are > 90%.

3. 2. 2 Neutron Diffraction

Neutron diffraction is an extremely powerful technique for the determination of magnetic ordering in materials on an atomic scale. Of all types of neutron scattering instruments in the world, diffractometers are by far the most common. The ordering pattern of the spins and the size of the ordered magnetic moment can be obtained from the data in a straightforward way unless the ordering is extremely complicated and exotic (in most of such cases neutron diffraction was used to prove that these structures exist). Magnetic neutron scattering (Shull et al., 1951a; Shull et al., 1951b) and polarized neutron diffraction (Mook, 1966; Moon et al., 1969; Moon et al., 1972; Moon and Koehler, 1975) were pioneered at Oak Ridge National Laboratory. Many diffractometers have been built which are optimized for magnetic scattering. Surprisingly, not many of them actually use polarized neutrons (see Nathans et al., 1959, for an early example). The reasons are that ① polarizing the beam significantly reduces the beam intensity, and ② in most cases it is sufficient to observe the *additional* scattering in reciprocal space while cooling the sample below the ordering temperature. In particular this is true for powder samples, where one averages anyway over all equivalent crystal directions. A microscopic model of the magnetic ordering can be developed that is compatible with the data, and in many cases the choice of the model will be unique. The symmetry of the spin structure is usually revealed by the presence or absence of specific reflections. For example, a collinear structure with moments aligned parallel to a (001) crystal axis has the signature of extinct (00l) reflections, because only spin components perpendicular to q are relevant for magnetic scattering.

There are, of course, cases where a polarized beam is indispensable for the determination of the magnetic structure of a material. These are usually single crystals with either a complicated ordering pattern (non-collinear ordering, chemically different magnetic ions in one unit cell etc.) or with a highly symmetric ordering which has only few reflections. The latter case may cause a problem because towards high q intensity is increasingly suppressed by the magnetic form factor.

One can distinguish two types of diffractometers which are dedicated to using polarized neutrons. A diffractometer such as D3 at ILL, Grenoble, France, shown in Fig. 3. 8a (see also http://www.ill.fr/YellowBook/D3) is built to study single crystals. In the past it has been used for the quantitative determination of magnetization distributions of magnetically ordered single crystals (Ressouche et al., 1993), for the investigation of exotic antiferromagnetic structures (Hiess et al., 2001), for the determination of antiferromagnetic form factors (Brown et al., 1999), and the search for spin liquids or short-range ordering in paramagnetic phases. D3 mostly uses hot neutrons and has $Co_{0.92}Fe_{0.08}$ and Heusler alloy Cu_2MnAl monochromator crystals. A ^{3}He neutron spin filter is currently being installed to analyze the scattered polarization which is significantly better than using a spin analyzer crystal.

D3 can host the CRYOPAD device (Tasset et al., 1999) which allows one to do spherical polarization analysis (see Fig. 3. 8b). This technique is experimentally challenging, because it requires zero magnetic field, and CRYOPAD is designed to make this possible without loss of beam polarization. The requirement of zero sample field can readily be seen.

Measuring off-axis terms of the polarization tensor $\hat{S}$ requires the incident polarization P and the scattered polarization P' to be set parallel to independent axes. While the incident polarization P would always be parallel to the field at the sample position, any component of the scattered polarization P' perpendicular to that field would precess around the field and the beam average of those components would therefore be zero. This precession is avoided if the sample field is sufficiently low. The diagonal terms of $\hat{S}$, on the other hand, can be measured with a non-zero sample field, because P and P' are parallel. The low-field sample chamber of CRYOPAD is made of two cylindrical superconducting Nb shields. These are transparent to neutrons and allow passing from guide field to zero field without significant loss of polarization. An experiment consists of measuring the scattered polarization with the incident polarization along each of the axes x, y and z. For each of the three incident polarizations, the scattered polarization is analyzed along all three spatial directions, so that all 9 elements of the polarization tensor $\hat{S}$ can be measured.
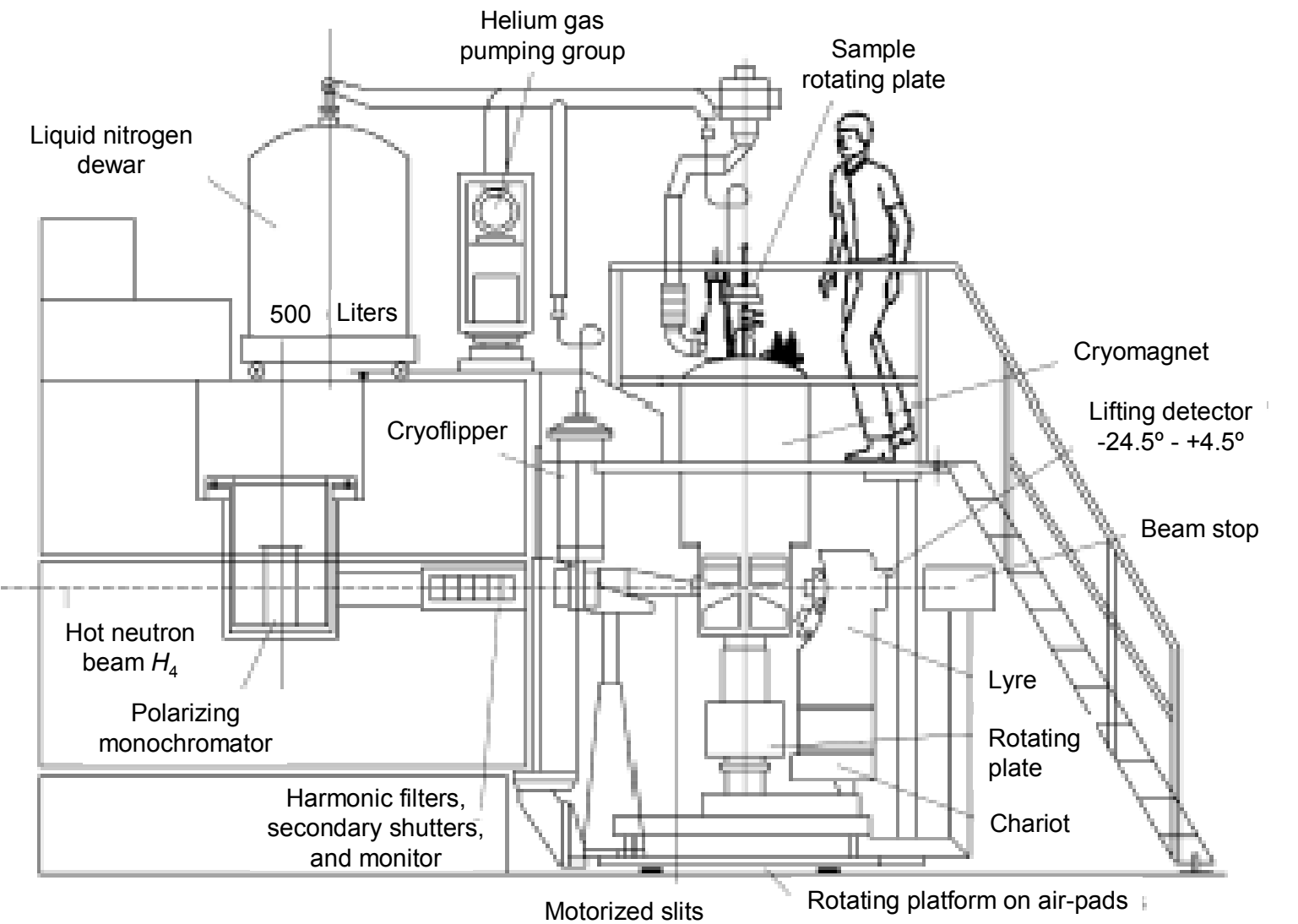

Figure 3. 8a   Schematic layout of the D3 diffractometer at the ILL (from D3 web site).
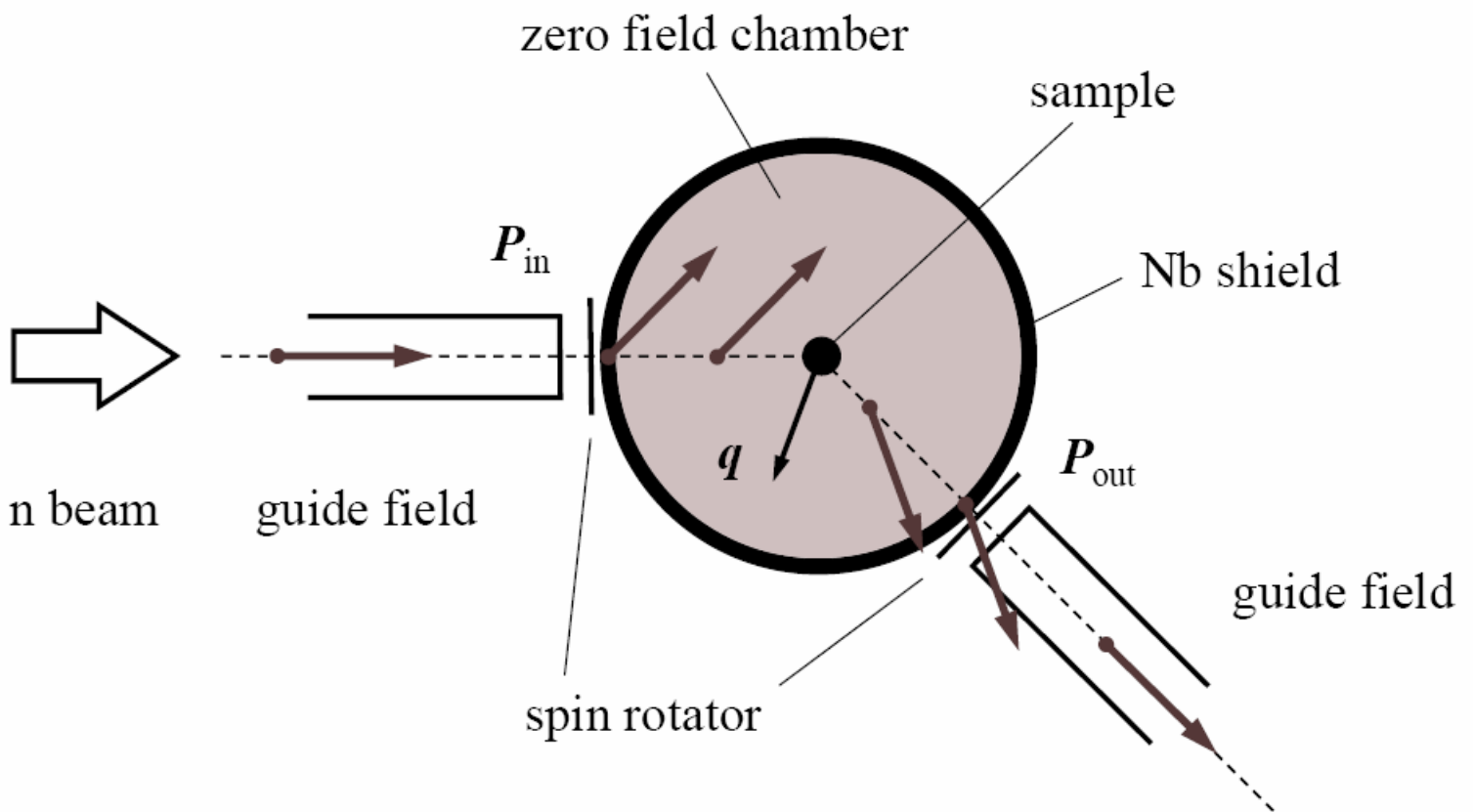
Figure 3. 8b   Schematic design of the CRYOPAD device (after Tasset et al., 1999).

A complementary type of diffractometer is D7 at ILL, Grenoble, France (see www.ill.fr/YellowBook/D7). This instrument is optimized for studying diffuse magnetic scattering (Stewart et al., 2000; Cywinski et al., 1999). Figures 3. 9 and 3. 10 show the general layout. A doubly-focusing graphite monochromator is used to define the incident energy. The beam then passes through a supermirror polarizer, a Mezei spin flipper and a disk chopper (the chopper is optional and allows for performing energy analysis of the scattered neutrons using the time-of-flight method). A removable set of six coils, wide enough for a furnace or orange cryostat to enter, is placed around the sample position in order to define the incident beam polarization direction (see Fig. 3. 9). D7 has four detector banks placed at 1.5 m distance from the sample. Each of the 32 single ^{3}He detectors has an individual supermirror spin analyzer. The necessary guide field between sample and analyzers is provided by permanent magnets. The instrument is flexible: Guide field and spin analyzers can be replaced by a radial collimator for measurements without polarization analysis. The following modes of measurement are possible:

(1) No polarization analysis: unpolarized neutrons in - no analysis after scattering;

(2) Polarized Neutron Diffraction: polarized neutrons in - no analysis after scattering;

(3) Z polarization analysis: two measurements (with and without spin-flip); allows the separation of coherent and incoherent scattering in non-magnetic systems;

(4) XYZ polarization analysis: six measurements; allows the separation into coherent, incoherent and magnetic contributions.

D7 is not only versatile for magnetic studies but is also used by other communities, because polarization analysis allows for separating coherent from spin-incoherent scattering, as for example, in polymers (Eilhard et al., 1999) or liquids (Garcia-Hernandez et al., 1999). A general overview of the applications of elastic scattering of polarized neutrons to study non-magnetic materials is given by Gabrys (Gabrys, 1999).
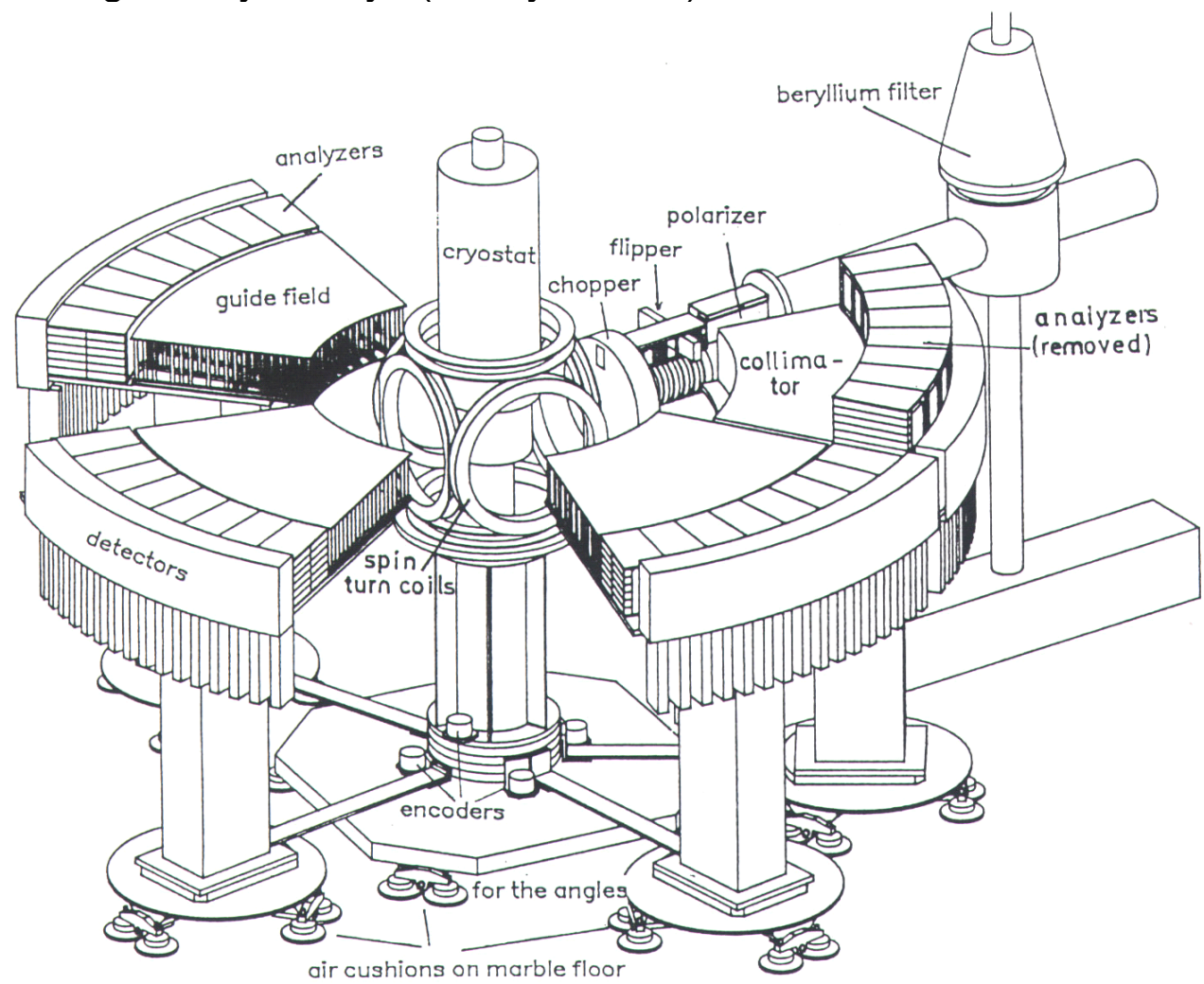
Figure 3. 9   General layout of the D7 polarized neutron diffractometer. The monochromatized neutron beam enters the instrument from the upper right corner through a beryllium filter that removes the unwanted higher order reflections of the monochromator. The sample is located in the center position inside a cryostat and is surrounded by four detector banks. The latter are mounted on air cushions to allow for variable scattering angle coverage.
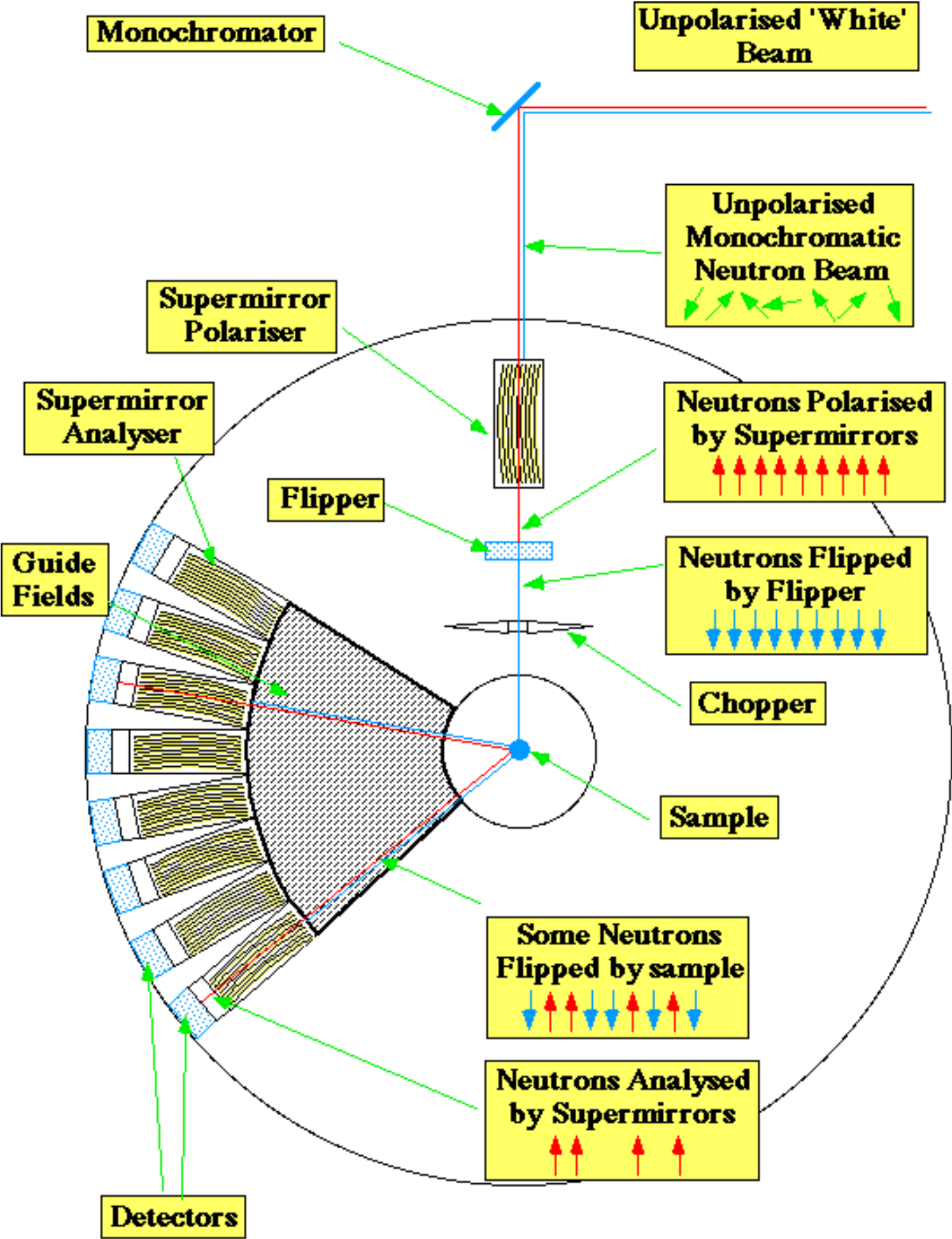
Figure 3. 10   Schematic layout (top view) of D7 for polarized neutron scattering experiments with polarization analysis (see text). The diagram shows only one of the four spin analyzing detector banks.

As an example for magnetic diffraction, we review the study on atomic and magnetic correlations in an archetypal spin glass CuMn, performed by neutron scattering on single crystals.

The term "spin glass" refers to the particular magnetic state of a system of spins with two basic ingredients: ① spatial disorder and ② frustration due to competing antiferromagnetic (AFM) and ferromagnetic (FM) interactions. Spatial disorder is, for example, realized in dilute solid solutions of magnetic

ions such as Mn or Fe in noble metals (CuMn, AgMn, AuFe are well studied examples), or by partially substituting a magnetic ion in a stoichiometric crystal (as in $Eu_xSr_{1-x}S$). The magnetic interactions can be of different origin. In non-metallic rare-earth compounds, the 4f electrons couple via direct isotropic Heisenberg super-exchange (EuS). In the case of 4f ions in metals the interaction is thought to be based on the Ruderman-Kittel-Kasuya-Yosida (RKKY) mechanism (Ruderman and Kittel, 1954; Kasuya, 1956; Yosida, 1957). The 6s conduction electrons (and in certain cases electrons in the partially overlapping 5d shells) are polarized by localized 4f moments, and neighboring 4f moments, in turn, are coupled via the polarized conduction band (it has to be said though, that the original RKKY model is far too simple and has seen numerous attempts to extend it to realistic cases). The main feature of the RKKY interaction is that it causes an oscillatory dependence of the coupling constant between two sites as a function of distance. In metallic spin glasses with 3d moments, the situation is very complicated and not fully understood. At low concentration of magnetic impurity (roughly below 10%), the moments are to a good extent localized and an RKKY type interaction can be assumed, but at high concentration the 3d moments become itinerant. It depends on how the magnetic ions are distributed and how the 3d states overlap. Magnetic anisotropy may also play a decisive role for the understanding of some systems.

Experimentally, the following phenomena are characteristic for spin glasses: ① a peak in the ac susceptibility $\chi_{ac}(T)$ at low temperature, the position of the maximum defining the spin glass temperature T_f, ② absence of magnetic Bragg peaks in neutron diffraction, meaning that the spins "freeze" randomly without long range order, ③ there is no anomaly in the magnetic specific heat at T_f but a broad bump at higher temperature (at about 1.3 T_f), ④ the magnetization shows a strong history dependence below T_f, and a slow non-exponential relaxation after perturbation.

In the CuMn system the situation gets even more complicated because atomic short range order is observed: Mn atoms are preferentially surrounded by Cu atoms. This is important as it has an influence on the distribution of Mn-Mn distances in a sample. Again, polarized neutrons give unique insight into this particular problem on an atomic scale, because one can look at magnetic and nuclear correlations at the same time in the same sample.

Neutron diffraction has contributed to this particular field from the very beginning (Meneghetti and Sidhu, 1957), showing the absence of long range magnetic order, except for a high Mn concentration above 70 at%. These early measurements did reveal broad magnetic "humps" situated between the (100) and (110) Bragg peaks, indicating short range ferromagnetic order. The centers of these humps were later identified as the (1, 1/2, 0) position (and equivalent positions) in reciprocal space. Experiments on single crystals later showed the existence of additional and somewhat sharper reflections at (1, 1/2 ± δ, 0) (Cable et al., 1982; Lamelas et al., 1995), which were attributed to "spin density wave" (SDW) like AFM correlations. The parameter δ depends on the Mn concentration and could be followed to very dilute systems with 1

at% Mn and even less. An extrapolation to zero Mn content gave a value for the position of these peaks well correlated with the Fermi wave vector $2k_f$ of Cu. The proposed interpretation of these findings was that CuMn alloys are incommensurate SDW antiferromagnets, with the magnetic order driven by the intrinsic instability on the Fermi surface of Cu (see Fig. 3. 11). This conclusion was opposing the widely accepted view of CuMn alloys as spin glasses.

Motivated by this controversy, a recent study on a single crystal of Cu-5at% Mn was performed at D7 at ILL (Murani et al., 1999, Stewart et al., 2000).
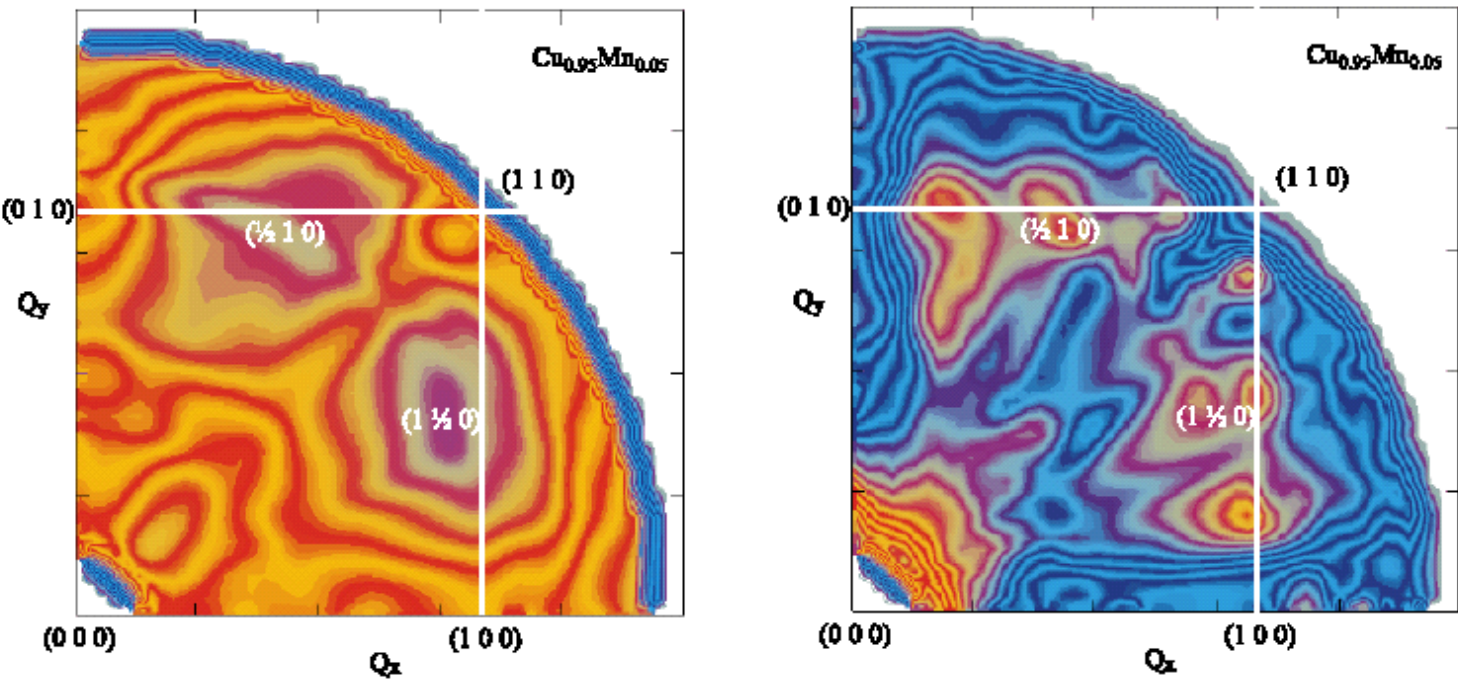

Figure 3. 11   Nuclear (left panel) and magnetic correlations (right) simultaneously measured by polarized neutron diffraction in a Cu-5at% Mn single crystal at low temperature (1.5 K). Data taken from Stewart et al., 2000.

These are probably the most precise elastic data available on CuMn. The earlier experimental findings are all confirmed: ① atomic short range order is seen by the broad intensity maxima around (1, 1/2, 0) and (1/2, 1, 0) in the nuclear correlation map, ② both the broad magnetic correlation peak at the same positions as well as the SDW peaks at incommensurate positions are found. Nevertheless the above interpretation is not forced, because these magnetic features actually represent only a small fraction of the total magnetic scattering intensity. One also observes a quasi uniform background present at all q, originating from the random freezing of most of the Mn spins. In addition, comparison to other available data shows that this "background" becomes more important as the Mn concentration decreases. Another strong argument supporting the spin glass view comes from the observation (Mezei et al., 2000) that the intensity of this scattering is very much temperature independent up to 100 K (the quasielastic width of the scattering function increases of course a lot with temperature) and its $q = 0$ limit corresponds well to the bulk susceptibility measured above T_f. Therefore it can be concluded

that SDW like AFM correlations coexist with the spin glass state but are not dominating the magnetic behavior of CuMn crystals at low temperature.

3. 2. 3 Reflection of Neutrons from Magnetic Surfaces and Interfaces

Polarized neutron reflectometry (PNR) has a successful track record of providing unique insights in problems of magnetic surfaces, thin films, interfaces, and multilayer systems [for a recent review, see for example (Ankner and Felcher, 1999)]. Areas of current fundamental science addressed by this technique include flux penetration and flux-lattice ordering in superconductors, nucleation and growth of structured surfaces, magnetic moment formation in thin films, interface polarization, interfacial coupling and quantum confinement, giant and colossal magnetoresistance. In the future, investigations on magnetic domains and patterned structures of magnetic dots or other nanoparticles, self-assembled layers and integrated materials such as polymers combined with magnetic materials, molecular magnets etc. will become increasingly important. Fundamentally new scientific insights gained by PNR were and will be important in the development of future thin-film based applications, such as new hard and soft magnetic materials to improve the efficiency of energy delivery systems (e.g. motors, transformers etc.) (Fullerton et al., 1999), magnetic recording media and magnetic sensors for computers (Speriosu et al., 2000; Thompson and Best, 2000), new magnetic memory technologies such as non-volatile magnetic random access memory (MRAM) and other so-called *spintronics* devices (Prinz, 1999).

Next generation instruments with much higher available neutron flux such as the Magnetism Reflectometer at the Spallation Neutron Source (Lee and Klose, 2001) will provide unprecedented experimental capabilities. Most importantly, they will be capable of routinely detecting weak off-specular scattering signals resulting from chemical/magnetic structures *within* the layer plane using off-specular/grazing-incidence small-angle scattering (GISANS) techniques (Mueller-Buschbaum et al., 1999; Felcher and te Velthuis, 2001). Such experiments are unreasonably slow on today's instruments. The SNS reflectometers will be the first neutron scattering instruments capable of directly detecting scattering signals (finite size oscillations, see Fig. 3. 13) from monolayer films. The high neutron flux will make possible in-situ structural or magnetic phase-diagram determinations as functions of thermodynamic parameters such as temperature, pressure, atmosphere, magnetic field etc. and will even provide the ability for time-dependent studies (e.g. pulsed magnetic, electric, light or other fields etc.) The availability of polarized neutrons and the polarization analysis capability suggest that the instrument will also be used for specific studies on non-magnetic thin film samples. Examples of the latter cases include contrast variation, incoherent background reduction and phase determination for direct inversion of

reflectivity data into real-space scattering-length density profiles (Schreyer et al., 1999).

Figure 3. 12 schematically displays the scattering geometry in PNR experiments. Note that a similar geometry also applies for general diffraction experiments with polarization analysis. A peculiarity of the thin film case is that the shape anisotropy usually forces the magnetic moments to lie within the plane of the surface. The lateral arrangement of the moments, however, is generally determined by other causes, for example resulting from crystalline anisotropies or exchange coupling energies. Therefore, in PNR experiments, magnetic fields $\boldsymbol{B_{ext}}$ are typically applied within the sample plane (e.g. along the y axis in Fig. 3. 12). The direction of $\boldsymbol{B_{ext}}$ also defines the polarization axis of the neutron beam. In polarized reflectometry experiments, one measures four different cross-sections as functions of the scattering vector $\boldsymbol{q}$. The scattering vector can be scanned in two different ways: reactor type instruments typically use monochromatized neutrons and vary the scattering angle, while spallation neutron source instruments use the time-of-flight method at a fixed angle of incidence to scan λ and consequently $\boldsymbol{q}$. R^{++} and R^{--} are the *non-spin flip* reflectivities (the first superscript characterizes the incident neutron polarization and the second the exit polarization; + corresponds to "spin-up", − to "spin-down", respectively). These cross-sections are sensitive to the chemical layering of the film structure as well as the magnetic moment component $\boldsymbol{M_{\parallel}}$ that is oriented *parallel* to the neutron polarization axis. Provided that no other causes are present that lead to spin-flip scattering (see Section 3. 1. 3), R^{-+} and R^{+-} are sensitive to magnetic
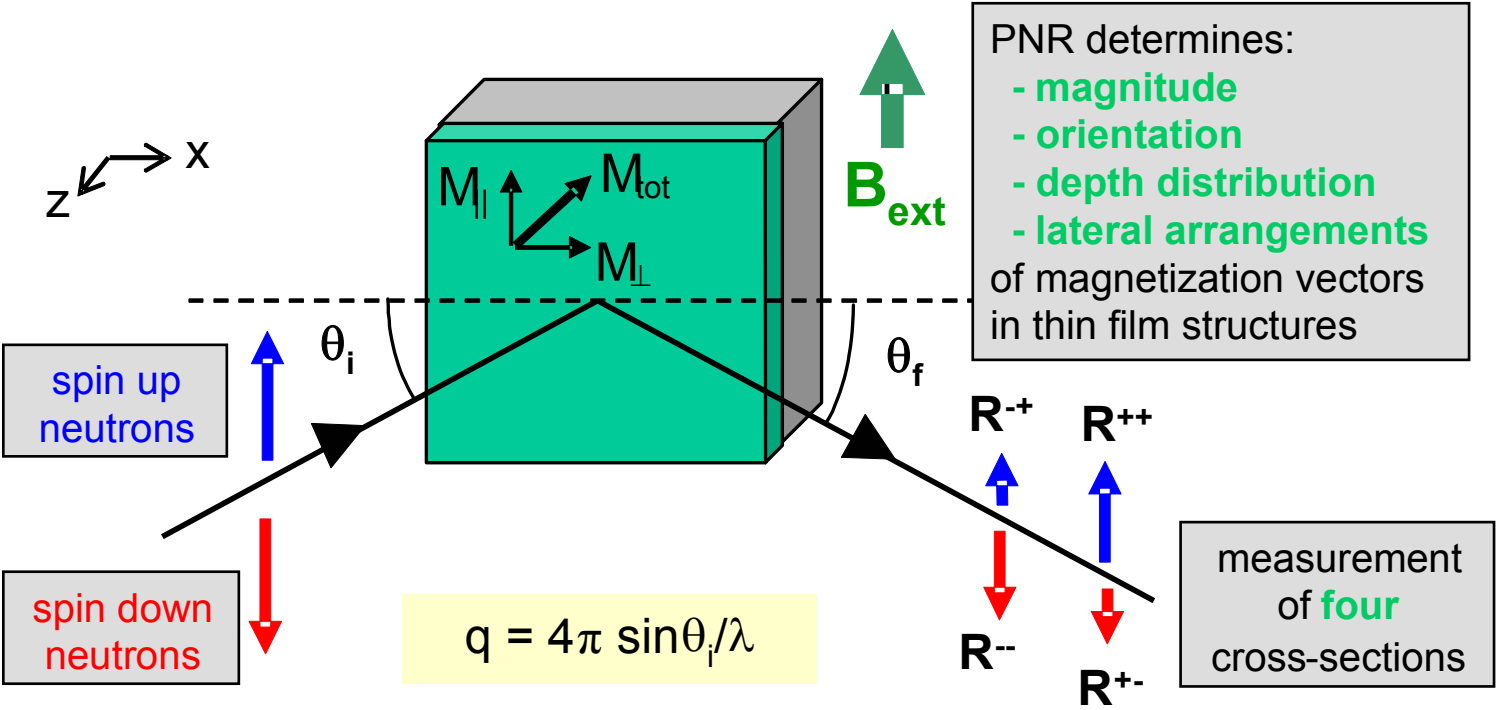

Figure 3. 12   Schematic representation of the scattering geometry in polarized neutron reflectometry experiments (see text). The thin film sample (green color) is usually deposited on a substrate material (grey). The magnetic moment vector $\boldsymbol{M_{tot}}$ may have components parallel and perpendicular to the neutron polarization axis.

moment components $M_\perp$ that are *perpendicular* to the neutron polarization axis (Zabel, 1994a). Therefore, PNR reveals not only the depth profile of collinear magnetic structures, but also allows studies of non-collinear magnetic arrangements, including chiral structures (O'Donovan et al., 2002).

Provided that the film is laterally homogeneous, the scattering is *specular*, i.e. the angle of incidence θ_i equals the take-off angle θ_f. In this case, reflectometry measures the chemical and magnetic depth profile along the *z* axis. In the first order Born approximation, the scattered intensity is given by (Als Nielsen, 1986)

$$I(q_z) \propto \frac{1}{q_z^4}\left|\int \frac{dV(z)}{dz}\exp(-iq_z z)dz\right|^2$$

where *V(z)* is the potential that the neutron experiences at a depth *z* inside the film. This means that the specular intensity is proportional to the square of the Fourier transformation of the gradient of the potential profile perpendicular to the surface. For a homogeneous layer consisting of a pure element, and with all its magnetic moments aligned parallel to B_{ext}, *V(z)* is constant throughout its depth and is given by

$$V = \frac{2\pi\hbar n}{m_n}(b \pm p)$$

In this expression, m_n is the neutron mass, *n* is the number density, and *b* (*p*) is the nuclear (magnetic) scattering length of the atom species, respectively. For spin-up neutrons, the magnetic contribution *p* has to be added to *b*, while for spin-down neutrons it has to be subtracted. For this particular case of aligned magnetic moments only R^{++} and R^{--} will have intensity. Since no perpendicular components of magnetic moments are present, no spin-flip scattering will occur and $R^{-+} = R^{+-} = 0$. Note that, in contrast to the diffraction regime, reflectivity is measured at low momentum transfer and, therefore, *V(z)* is a locally averaged potential. In the case that the material consists of different atomic species, their individual contributions to the average local potential have to be summed up. For a sequence of layers, *V(z)* changes continuously along the depth of the film.

It is well known that the Born approximation fails for $q_z \to 0$ (the intensity would become infinite at $q_z = 0$). In this regime, optical methods need to be applied that correspond to full dynamical theory taking multiple scattering, refraction and absorption effects into account (Majkrzak, 1991; Zabel, 1994b). A particularly useful method is the recursion scheme of Parratt (Parratt, 1954). This method does not contain approximations and provides exact solutions for reflectivity profiles. Interface roughness can be simulated by slicing the interface region in arbitrarily small regions that approximate the gradient of the potential.

Figure 3. 13 displays PNR spectra of typical thin film structures. The reflectivity functions have been calculated using the *Parratt 32* program developed by C. Braun, Hahn-Meitner Institute Berlin. For all film structures, the region of total reflection and the overall intensity is different for the R^{++} and R^{-} cross-section. While the reflectivity functions of the Fe surface are featureless declining proportional to $1/q^4$, the interference between partial waves reflected by the vacuum/film and film/substrate interfaces causes an oscillatory behavior of the reflectivity for the 500 Å Fe film (*Kiessig fringes*). The main feature of the multilayer reflectivity function is that strong Bragg peaks occur, which are resulting from the 80 Å double-layer thickness (50 Å Fe + 30 Å Nb).
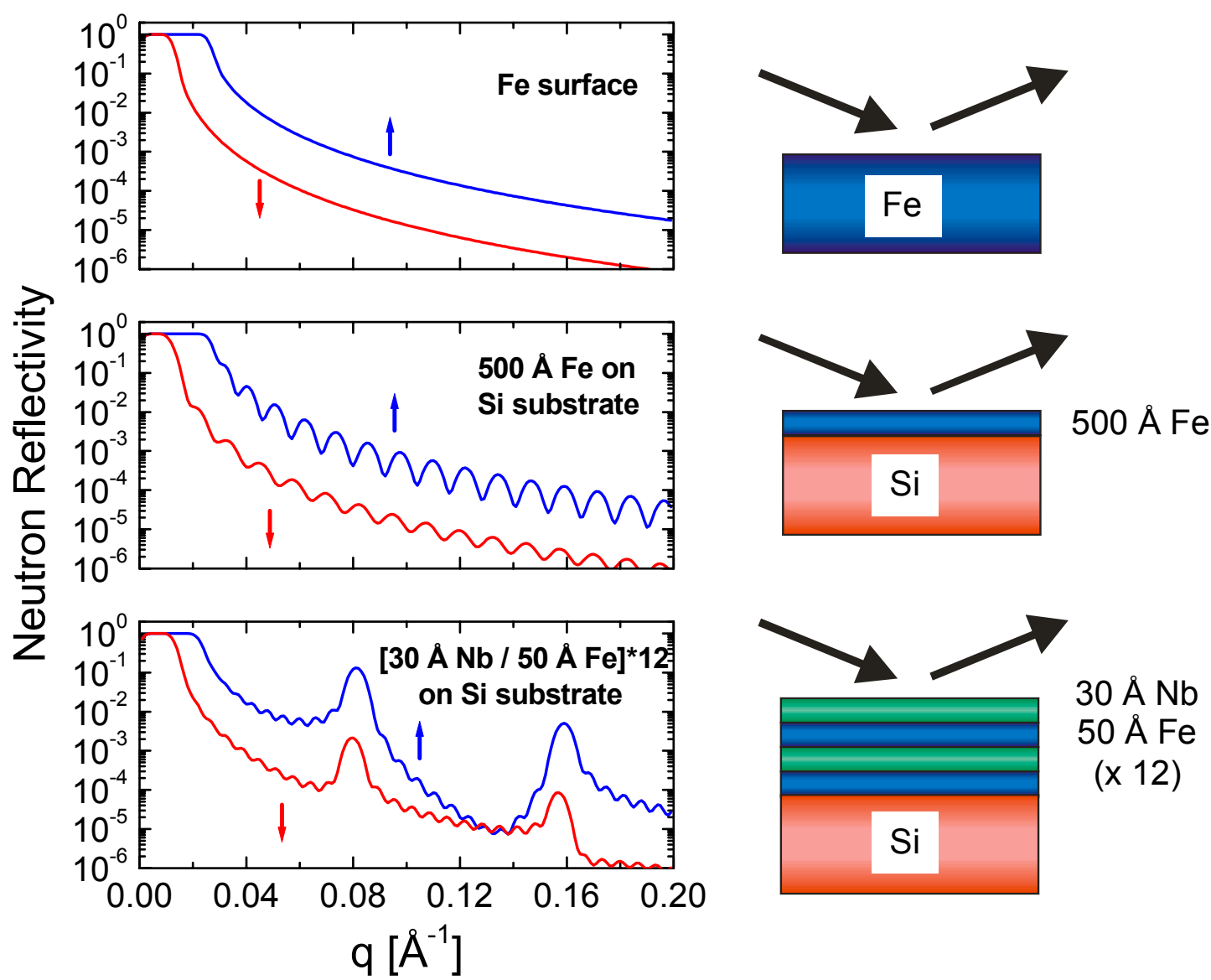

Figure 3. 13   Calculated PNR spectra for different layer sequences. Upper data set: a bulk Fe surface; middle: a 500 Å Fe film on Si substrate; bottom: a multilayer consisting of 30 Å Nb / 50 Å Fe with 12 repetitions on Si substrate. In all cases it is assumed that the magnetic layers are saturated along the magnetic guide field B_{ext}. R^{++} is plotted in blue and R^{-} in red color.

As mentioned above, laterally structured magnetic films become an increasingly more important research topic. Figure 3. 14 summarizes a neutron scattering experiment on a patterned magnetic film (Lee et al., 2003). The data were collected using the *POSY2* time-of-flight neutron reflectometer at Argonne National Laboratory. In this experiment, the sample consisted of lithographically produced rectangular Ni stripes of 10 µm × 2 µm area and 100 Å thickness that are separated by 2 µm from the neighboring stripes. A Si wafer serves as substrate. The scattering pattern displayed on the right side is typical for this kind of sample and demonstrates the usefulness of the technique. It shows specularly reflected intensity, where the final scattering angle θ_f is constant with wavelength (red arrow) and additional off-specular intensity fringes (blue arrows) that are located below and above the specular intensity. The fringes are extending along lines given by the solutions

$$2\theta = \theta_i + \sqrt{\theta_i^2 + 2n\lambda / d}$$

of the Bragg equation $q_x = 2\pi n / d$ for the two first-order ($n = \pm 1$) diffraction above the horizon, where d is the periodicity of the surface pattern along the flight path of the neutron (4 µm in the above case). Note that, since the substrate is largely transparent for neutrons, also a transmitted refracted
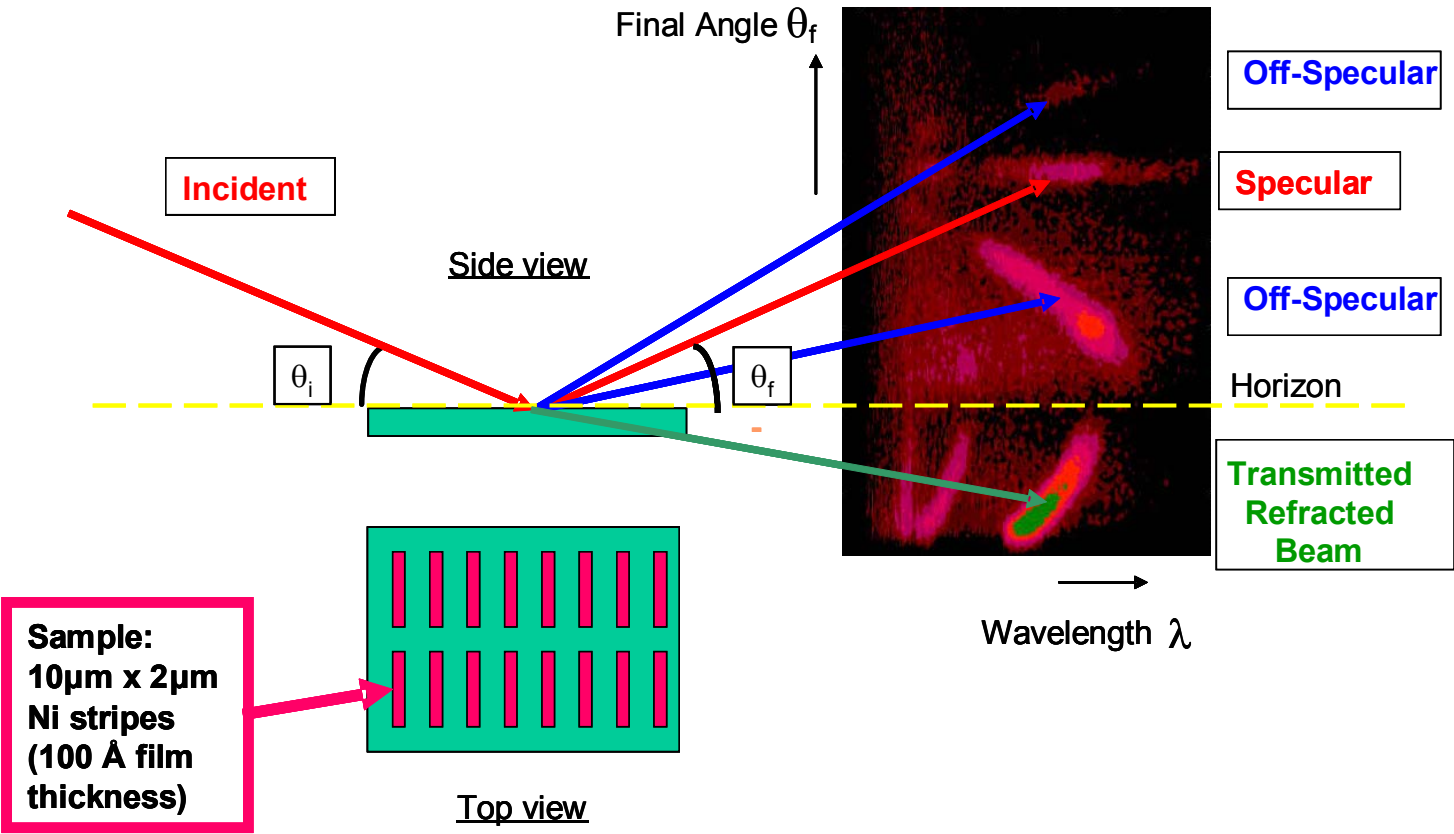

Figure 3. 14   Neutron reflectivity in time-of-flight mode on a patterned magnetic film structure. The left side shows the experimental arrangement and schematically the patterned surface in side and top view. On the right, the corresponding scattering pattern (contour intensity plot of final scattering angle vs. neutron wavelength) is displayed (Lee et al., 2003).

beam is visible below the scattering horizon. Analyzing such scattering surface pattern is not known from the outset, for example in the case of self-assembled structures. Magnetic information also can be obtained by using polarized neutrons and polarization analysis. For example, for the case of the Ni stripes, it allows to determine details of the magnetization reversal process. In particular, it permits distinguishing between domain reversal by a rotation or along a particular axis along the surface (Temst et al., 2001).

If the lateral length scale of the surface structure is large compared to the lateral coherence length of the neutron beam (the latter is typically on the order of microns to tens of microns), there is practically no off-specular intensity and no information on the size of lateral structure is available. Nevertheless, polarized neutron *specular* reflections may contain information on the lateral arrangements of large-scale magnetization inhomogeneities, such as large domains. Lee et al. recently measured the field dependence of the ferromagnetic domain dispersion χ^2 of an exchange biased CoO/Co bilayer film and demonstrated the possibility to extract information on the lateral distribution of magnetic domain orientations (Lee et al., 2002).

In the following, we describe an experiment that clearly demonstrates the advantages of using neutron scattering for characterizing magnetic phenomena in surfaces and thin films. In this example, *exchange coupling* in magnetic layered structures was studied. This effect, initially observed by Grünberg et al. in Fe/Cr multilayers (Grünberg et al., 1986), is of large impact on information technology due to the related *giant magnetoresistivity* (GMR) effect, which has been found in several material combinations. GMR is an extraordinary large change (up to 100%) of the electrical resistance of antiferromagnetically coupled thin film structures upon application of an external magnetic field (Baibich et al., 1988). GMR materials have quickly found various technical applications and are nowadays used for example as advanced sensor elements in read heads of computer hard disks.

Generally, exchange coupling of two magnetic layers through a non-magnetic spacer layer can be described by using RKKY-like or quantum interference models. Theoretically as well as experimentally, it is found that the coupling energy *J*, which is a measure of the coupling strength, oscillates approximately as

$$J \propto \frac{1}{(2\,k_F\,t_S)^2} \sin\left(2\,k_F\,t_S\right)$$

where k_F and t_S are the (effective) Fermi wave-vector and the thickness of the non-magnetic layer, respectively. According to the formula, exchange coupling is oscillating in sign, i.e. with increasing spacer layer thickness t_S, alternating ferro (FM)- and antiferromagnetic (AFM) coupling should be observed. This dependence of the exchange energy on the spacer layer thickness has been extensively studied in many systems, but surprisingly, only very few papers existed in the literature dealing with a manipulation of the Fermi wave-vector.

The main idea of the described experiment (graphically summarized in Fig. 3. 15) was to use hydrogen absorption for changing the electronic properties of the spacer layer material, including its Fermi wave-vector k_F, and demonstrate that this can result in a complete reversal of the magnetic coupling (Klose et al., 1997). Fe/Nb multilayers were chosen for these experiments because oscillating FM/AFM coupling had been positively identified (Rehm et al., 1997) and Nb, as the spacer layer, has a high solubility for hydrogen [experiments with similar results have been carried out by Hjörvarsson et al. on single-crystalline Fe/V superlattices (Hjörvarsson et al., 1997)].

Figure 3. 16a shows neutron reflectivity data of Fe/Nb multilayers, each with constant Fe thickness of 26 Å but with four different Nb thicknesses. These different chemical periodicities result in structural Bragg peaks as indicated in the figure. The samples were measured in their virgin state in "zero" external magnetic field because, due to the relatively small coupling strength in the Fe/Nb system, even small magnetic fields would possibly have affected the measurements. Therefore, unpolarized neutrons were chosen which made the use of a guide field unnecessary.
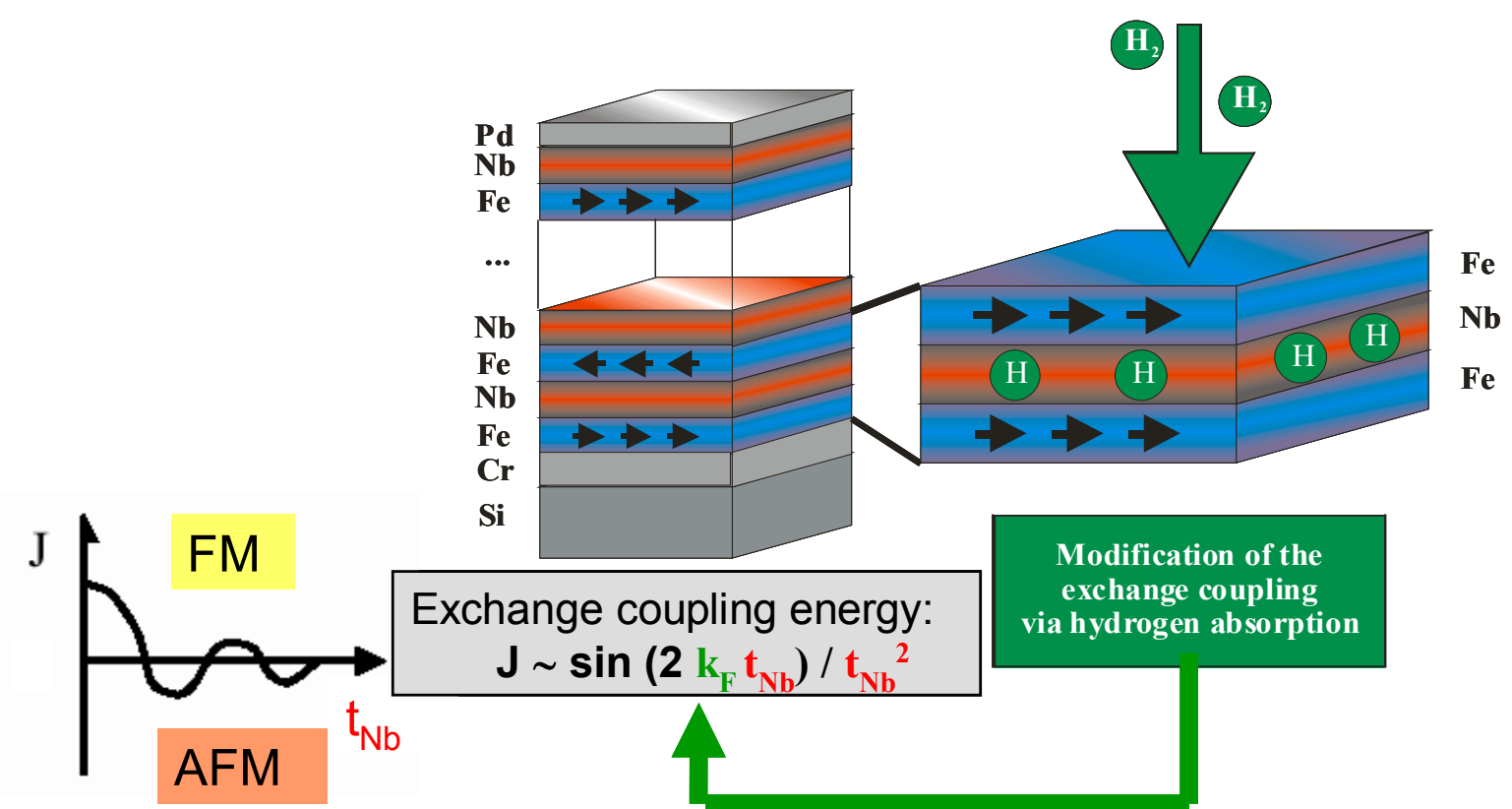

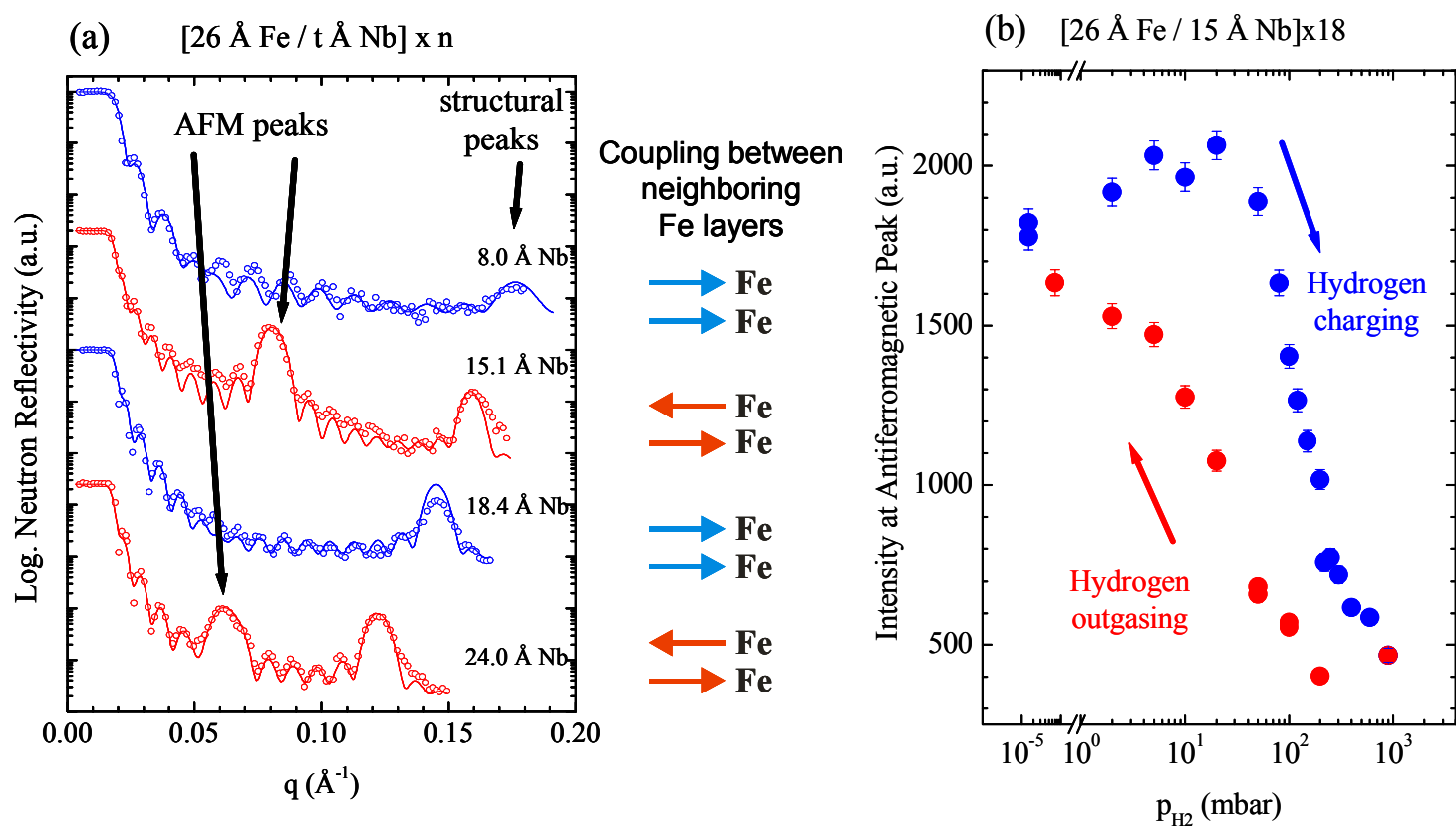Figure 3. 15   Hydrogen charging of Fe/Nb multilayers and resulting reversal of the magnetic coupling J.

Figure 3. 16   (a) Neutron reflectivity on Fe/Nb multilayers [26 Å Fe / t Å Nb] x n (t is the Nb layer thickness and n the repetition number). Note the extra half-order peaks at $\approx$ 15 Å Nb and $\approx$ 24 Å Nb, which indicate antiparallel coupling of neighboring Fe layers (Rehm et al. 1997); (b) Intensity of the antiferromagnetic Bragg peak of the multilayer [26 Å Fe / 15 Å Nb] x 18 (second data set from the top in (a)) as a function of the external hydrogen pressure. Blue symbols correspond to increasing, red symbols to decreasing hydrogen pressure (Klose et al. 1997).

Figure 3. 16a gives clear evidence that the magnetic coupling energy oscillates in sign. With increasing Nb layer thickness, the extra half-order peak resulting from coherent AFM coupling of neighboring Fe layers is visible only for $\approx$ 15 Å Nb and $\approx$ 24 Å Nb, but not for $\approx$ 8 Å Nb and $\approx$ 18 Å Nb (in the latter cases, intensity from ferromagnetic coupled Fe layers add to the intensities of the structural Bragg peaks).

The multilayers were charged with hydrogen from the gas phase in a vacuum chamber around the sample position of the neutron reflectometer at a temperature of 473 K (the hydrogen concentration in the Nb layers is a function of the external hydrogen pressure). This allowed an *in-situ* observation of changes of the magnetic coupling during the hydrogenation. Figure 3. 16b shows the development of the AFM intensity for the [26 Å Fe / 15 Å Nb] x 18 multilayer upon hydrogen absorption. It can be seen that the AFM intensity (and therefore the AFM coupling of the Fe layers) is strongly suppressed with increasing hydrogen content in the Nb layers indicating that FM coupling starts to dominate. It is interesting to note that this effect is completely reversible (although with a strong hysteresis effect) upon lowering the hydrogen concentration in the Nb layers by evacuation of the hydrogen in the loading chamber. The observed effect can possibly be used to fine-tune the magnetoresistive properties of GMR sensors or to build hydrogen sensors based on the GMR effect.

3. 3   Inelastic Magnetic Scattering

3. 3. 1 Studies of Elementary Excitations by Triple-axis Spectroscopy

Triple-axis spectroscopy (TAS) and chopper spectroscopy are both very effective techniques for detecting spin dynamics in magnetic crystals (Shirane et al., 2002, and references therein). Important scientific areas that can be investigated using these methods include strongly correlated electron systems (Hayden et al., 2000), high temperature superconductors (Aeppli et al., 1997), colossal magnetoresistive materials (Adams et al., 2000; Argyriou et al., 2002), low-dimensional magnets (Raymond et al., 1999), quantum and molecular magnetism (Hennion et al., 1997), and itinerant magnets (Boeni et al., 1990; Lynn et al., 1994). Chopper spectrometers have been built at reactor sources but are most effective at pulsed sources (Windsor, 1981, and references therein). In the latter case, typically a fast spinning *Fermi chopper* creates bursts of monochromatic neutrons. The energy of these neutrons can be varied by changing the phase between the Fermi chopper and the accelerator. Neutron energy changes during the scattering process are detected by measuring the time-of-flight between sample and detector. Chopper spectrometers can very effectively scan large areas in (q, ω) space using detectors with large solid angle coverage. Polarized neutron experiments, however, are technically very difficult for this type of instrument because of the relatively high neutron energies and the required large solid angle detector coverage. Only the recent progress in the development of ^{3}He spin-analyzing cells (see Section 3. 1. 2) opens realistic possibilities here.

The triple-axis spectroscopy method can be favorably combined with polarization techniques. An example for such instrument type is the IN20 spectrometer at ILL (see Fig. 3. 17).
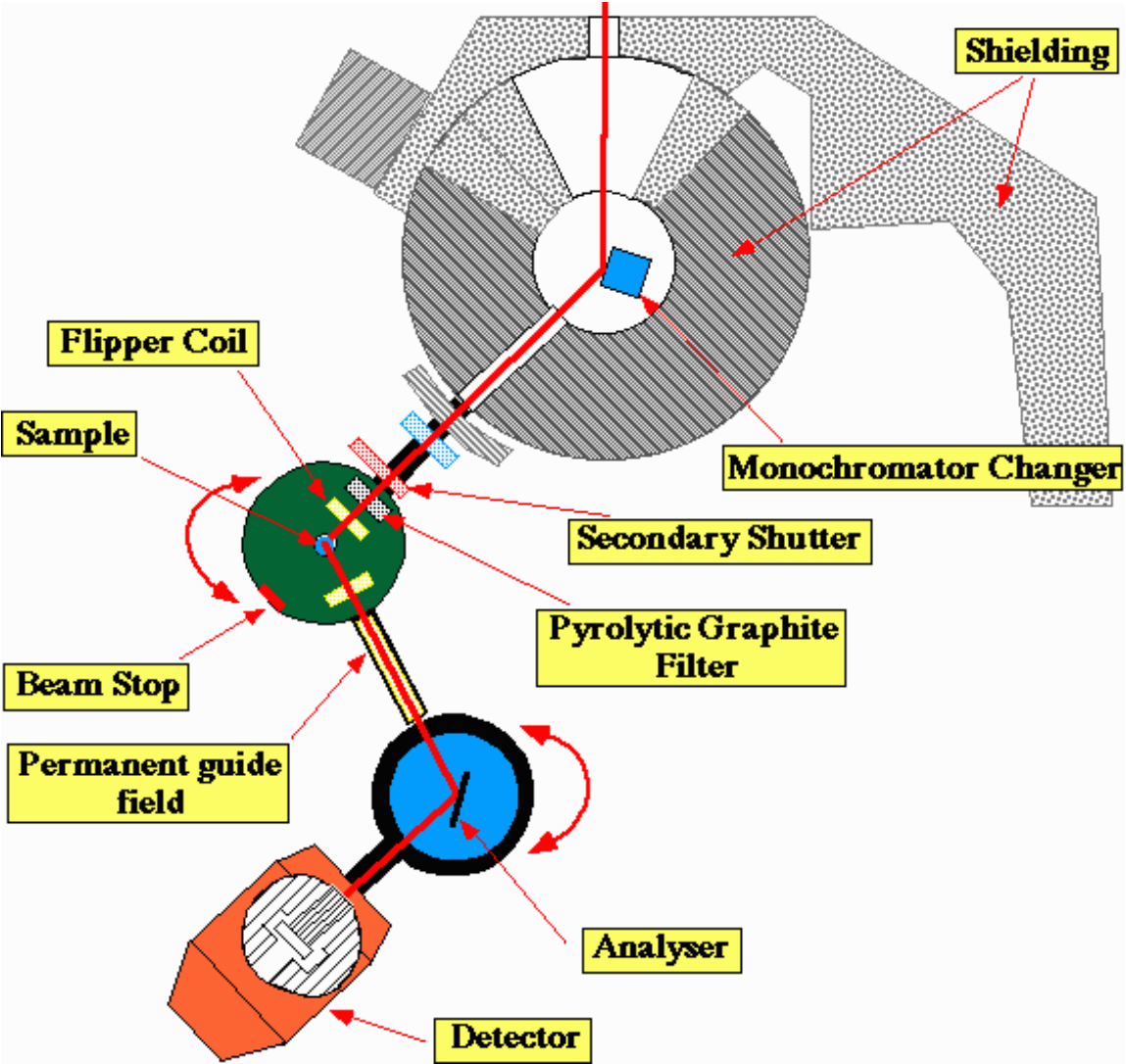
Figure 3. 17   Schematic layout of the IN20 triple-axis spectrometer at ILL. A combination of Heusler-alloy (Cu_2MnAl) (111) monochromator and analyzer (horizontally focusing) and two Mezei-type spin flippers allows polarization and analysis of the incident and scattered beams parallel or antiparallel to the vertical axis. The figure is taken from ILL web site (http://www.ill.fr/YellowBook/IN20/).

In triple-axis spectroscopy one compares the neutron momentum and energy before and after the sample, determined on either side by Bragg diffraction from monochromator and analyzer crystals. The principle is schematically shown in Fig. 3. 18.
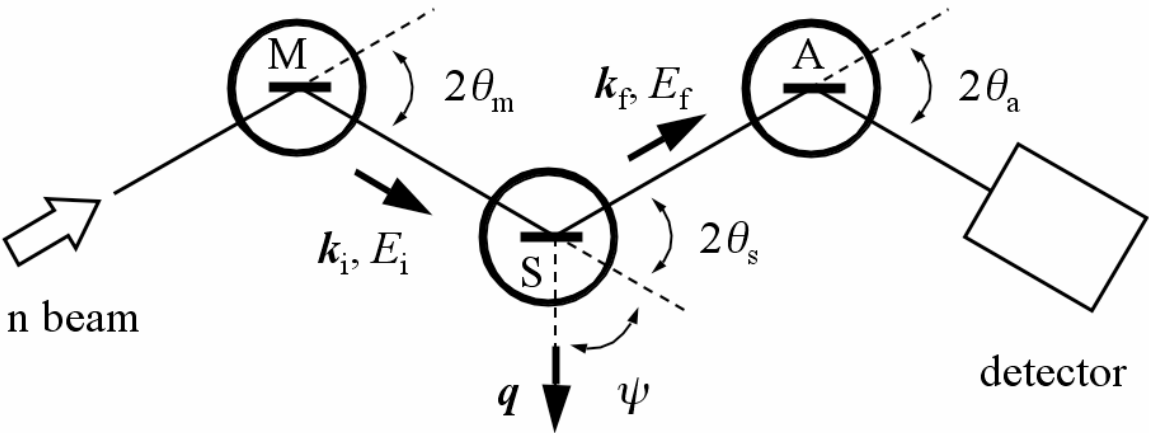

Figure 3. 18   General schematic layout of a triple-axis spectrometer. M, S, and A denote monochromator, sample, and analyzer, respectively. The angle ψ defines the crystal orientation in the laboratory frame. E_i, k_i and E_f, k_f are neutron energy and momentum before and after the scattering process with the sample, respectively (for details see text).

The incident white beam is reflected (at an angle $2\theta_m$) from a focusing monochromator crystal onto the sample. The neutron energy E_i and momentum k_i incident on the sample depend via Bragg's law on lattice spacing used in the monochromator and the angle θ_m. Focusing is usually vertical to increase intensity at the expense of vertical q-resolution. The choice of the monochromator mainly depends on the wavelength, as was discussed in Section 3. 1. 2. In the thermal and cold ranges, the (002) reflection from pyrolytic graphite yields the highest intensity. Cold neutrons are usually polarized in a second step by means of a supermirror polarizer. In the thermal and hot ranges one also uses Si (111), or various reflections from Cu, such as (111), (200) and (311). Heusler (111) crystals are used for direct beam polarization (see Section 3. 1. 2), mainly in the thermal neutron range, as for example at the IN 20 spectrometer (see Fig. 3. 17). The beam scattered from the sample at an angle $2\theta_s$ is reflected from an analyzer crystal into the detector. The angle θ_a at the analyzer determines the neutron momentum k_f and energy E_f after the sample. Collimators may be placed in the flight path to reduce the angular divergence of the beam and improve q-resolution. Filters are often used to reduce intensity of contaminant short wavelength neutrons.

Each experiment measures the scattering function $S(q,\omega)$ along certain lines in (q,ω) space, where $q = k_i - k_f$ and $\hbar\omega = E_i - E_f$. In the horizontal plane the scattering function has three independent parameters (ω and two horizontal components of q), while there are four adjustable observables: the energies E_i and E_f, the scattering angle $2\theta_s$ and the angle ψ which defines the crystal orientation in the horizontal plane of the laboratory frame. Usually one keeps either E_i or E_f constant during a particular scan.

The accessible ranges of energy and momentum transfer depend on the incident wavelength: using cold neutrons, one can typically measure up to $\hbar\omega = 10 meV$ and $q = 5$ Å^{-1}. While using thermal neutrons, the energy range is 10 times larger and the q range is about 2.5 times larger. The spectrometer resolution in both energy and q is typically a few percent but depends on the collimation and monochromatization of the beam: higher resolution means less flux and smaller count rate in the end. Modern spectrometers are flexible to allow adapting the experimental conditions to the resolution requirements of any particular experiment as much as possible. This flexibility is one of the strongest points of triple-axis machines.

Spectrometers which are built for the study of magnetic systems profit very much from the ability to use polarized neutrons (about 1/3 of all spectrometers in the world either have this capability as an option or use it all the time). Polarization handling on a triple-axis instrument is straightforward: one typically uses permanent magnets creating a vertical guide field along the spectrometer arms and an arrangement of Helmholtz coils for the sample region to control magnitude and direction of the field at the sample position. In real experimental conditions typical flipping ratios in the beam incident on the sample ($k_i = 2.7...4$ Å^{-1}) are in the range between 10 and 20. The option to change the field direction with respect to q is important: As we have seen in

the theory Section 3. 1. 1, the effect of magnetic scattering on the scattered beam polarization depends on the relative orientation of sample field and $\boldsymbol{q}$.

An example that we would like to highlight is the inelastic scattering work performed on the germanate $CuGeO_3$. It shows the particular value of polarization analysis in neutron scattering.

$CuGeO_3$ is the first inorganic compound found to show a "spin-Peierls" phase transition, which takes place below $T_{SP} \approx 14$ K (Hase et al., 1993; Boucher and Regnault, 1996). This means that linear chains of antiferromagnetically coupled Cu^{2+} ions, which are parallel to the c axis, show intrachain dimerization at low temperature: the Cu^{2+} ions are slightly displaced along the chain direction to form pairs of nearest neighbors. This effect was predicted for one-dimensional Heisenberg or XY antiferromagnetic s=1/2 spin chains, where at low temperature large quantum fluctuations give rise to a broad continuum of excitations (Müller et al., 1981). These fluctuations induce the lattice distortion via strong spin-phonon coupling. Experimentally, the spin-Peierls transition has been found by measuring the magnetic susceptibility of a crystal in applied fields parallel to the different crystal axes, and has been confirmed by specific heat, X-ray and neutron diffraction, Raman scattering and electron spin resonance (ESR) measurements. A third phase that appears in high magnetic fields above 12.5 T has been identified in which the whole lattice becomes incommensurate (Kiryukhin et al., 1996). Figure 3. 19 shows the (B,T) phase diagram of $CuGeO_3$ (Boucher et al., 1996).
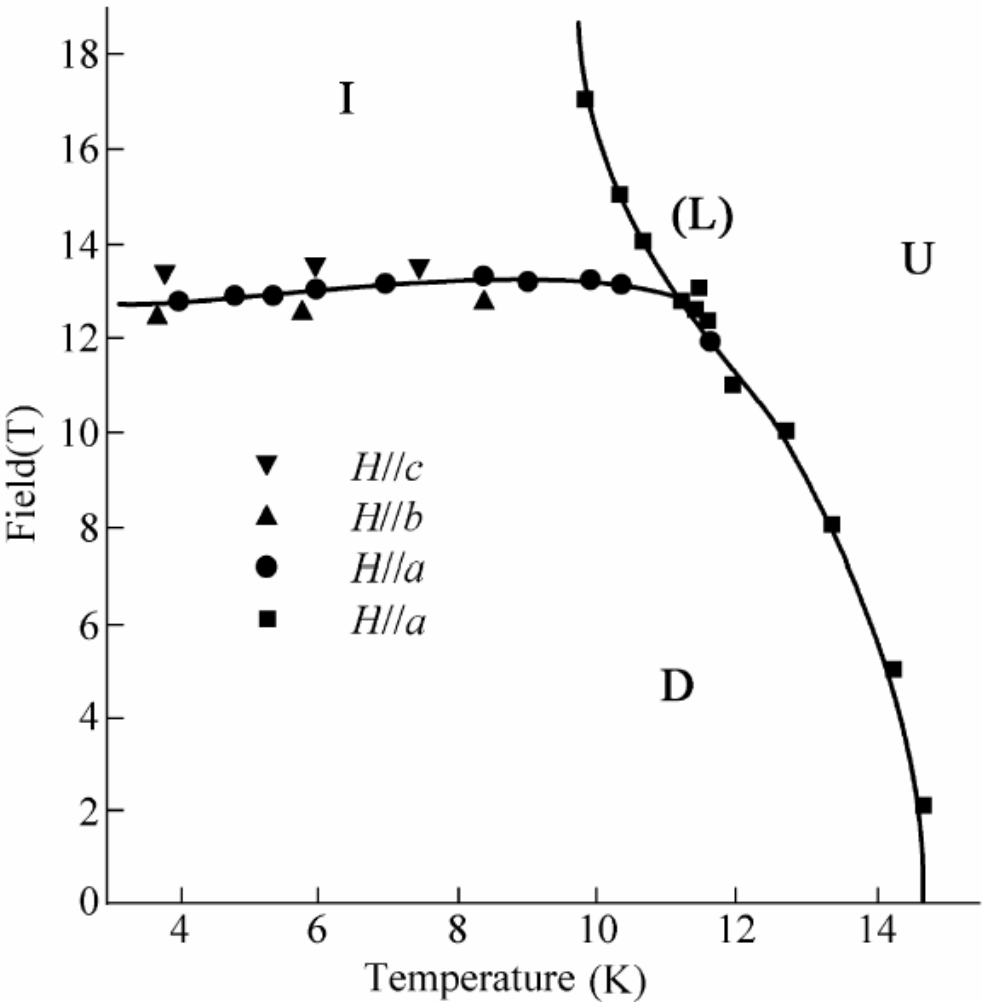

Figure 3. 19   (B,T) phase diagram of $CuGeO_3$ showing the three different phases: uniform (U), dimerized (D) and incommensurate (I). Solid and dashed lines are second and first order transitions, respectively. (L) is a Lifshitz point. (Boucher et al., 1996)

The inelastic polarized neutron scattering work has significantly contributed to our understanding of $CuGeO_3$ by measuring the structural and magnetic excitations in the low-field phases. This has revealed some peculiarities which are not accounted for by the standard theoretical approach. For example, while in the dimerized phase there is an energy gap in the spectrum of the magnetic excitations as expected ($\Delta_{SP} \approx 2$ meV), this gap does not vanish at the critical temperature T_{SP} (Regnault et al., 1996). This was attributed to the persistence of a "pseudo gap", broad inelastic scattering present above T_{SP} and peaking at finite energy transfer. In the non-spin-flip scattering (which should contain only nuclear scattering) the scattering contribution at Δ_{SP} is also visible, even after correction to the finite beam polarization. This means that at this position in energy space the magnetically and inelastically scattered neutron suffers an additional change of its polarization, either a depolarization or a rotation around the sample field. As we have seen in Section 3. 1. 3, three-dimensional polarization analysis can not distinguish between these two cases.

An experiment using spherical polarization analysis was performed later to elucidate this finding (Regnault et al., 1999). It was found that some off-diagonal elements of the polarization tensor, which can be determined by this method, are non-zero at [q=(0,1,1/2), $\hbar\omega = 2meV$], whereas no polarization in the scattered beam appeared when the incident beam was depolarized, which altogether was consistent with the earlier experiment, proving a non-trivial *rotation* of the final beam polarization due to the scattering. What does this mean? In the off-diagonal elements, terms appear that couple nuclear and magnetic scattering amplitudes. In an inelastic experiment these are correlation functions which couple the time-dependences of the spin components perpendicular to q and the time-dependences of atomic displacements parallel to q at the same site and the same time. Hence one can qualitatively conclude that the low-energy excitations observed in $CuGeO_3$ are "dual entities" with both spin and lattice degrees of freedom (Regnault et al., 1999).

3. 3. 2 Detection of Slow Motions by Neutron Spin Echo

Neutron spin echo (NSE) is a technique that uses polarized neutrons to achieve very high resolution for measuring the neutron energy transfer in the scattering process. Its main applications are found in *quasielastic* scattering experiments (excitation centered around zero energy transfer). Contrary to other inelastic techniques such as TAS, it measures the intermediate correlation function in reciprocal space and time $I(q,t)$. The time window spans from 10^{-12} s to 10^{-7} s, partly overlapping with the μSR technique that can detect even slower spin dynamics but has no q information. NSE is rather unconventional in the sense that q- and E-resolutions are completely decoupled and one does not have to trade beam intensity for energy resolution. Compared to TAS, spin echo measures at longer times (smaller

energy transfer). Traditionally it is a domain of soft matter physics and chemistry and only few magnetic systems were studied in the past. Review articles on the spin echo method are available, with emphasis on applications in soft (Ewen and Richter, 1997) and condensed (Mezei, 1993) matter physics. The most comprehensive references, with many applications, are the books *Neutron Spin Echo* (Mezei, 1979; Mezei et al., 2003).

The functioning of a spin echo spectrometer can be described as follows (see Fig. 3. 20). The beam is monochromatized to typically $\Delta\lambda/\lambda \approx 15\%$ by a velocity selector. The basic idea of NSE is to compare the ingoing and outgoing neutron velocities (before and after the scattering event, respectively) by using the Larmor precession of the neutron spin in a magnetic field (compare Section 3. 1. 2). The magnetic field is parallel to the beam direction and is created in long solenoids. NSE uses a cold neutron beam that is polarized by a supermirror transmission polarizer. After the polarizer, the beam passes a Mezei spin flipper that acts as a $\pi/2$ flipper: when the neutron exits the flipper, its spin points perpendicular to the field
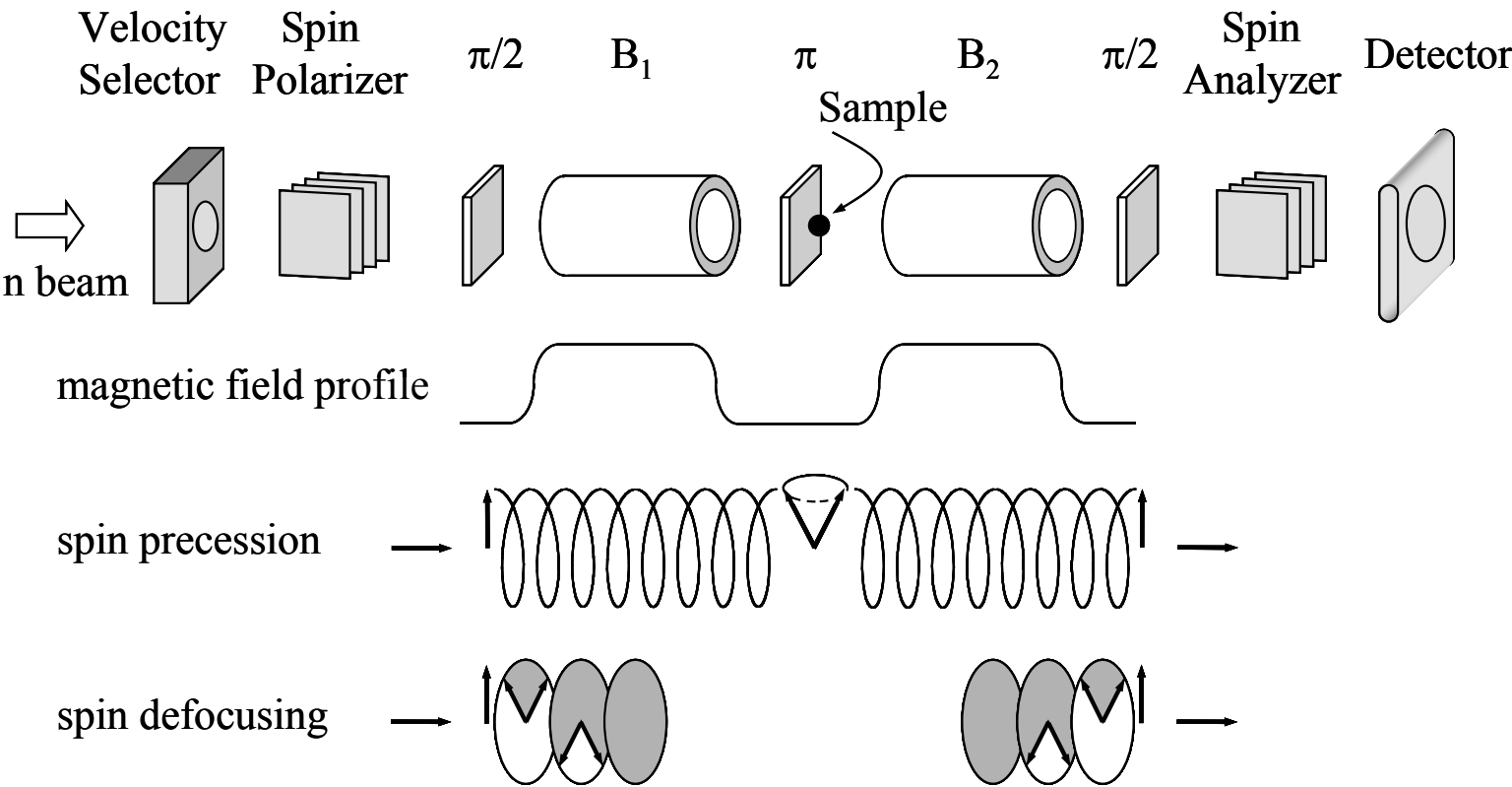

Figure 3. 20   Layout of a generic NSE spectrometer. Top row: The beam enters on the left side. The beam passes a velocity selector, spin polarizer, $\pi/2$ flipper, precession field B_1, π flipper, sample, precession field B_2 (note that the fields B_1 and B_2 are parallel), $\pi/2$ flipper, spin analyzer, detector. The second row shows the corresponding magnetic field profile. The third row demonstrates the manipulation of an individual neutron spin. The fourth row schematically shows the defocusing of the spins due to the velocity spread of the neutrons. At the first $\pi/2$ flipper, all spins point in the same direction, but they refocus on the secondary side only if the product Bl/v is the same on both sides (see text). The sample (black dot) is centered between the precession fields B_1 and B_2.

direction. The neutron now enters a region with a high magnetic field B_1 and on its way to the sample the spin makes a total number of precessions given by

$$N_1 = \frac{\lambda}{135.65} \cdot \int B_1 dl$$
,

where λ is in Å and the integral over the modulus of the field (in G·cm) is to be taken between the $\pi/2$ flipper and the π flipper. In modern spectrometers the number N_1 can be as high as 2×10^4. Note, that due to the wavelength spread, N_1 is different for each individual neutron, so that the beam gets dynamically depolarized after a short travel distance in the precession field. Note that all neutron spins are still polarized in the plane perpendicular to the direction of the magnetic field. The π flipper turns the spin around an axis perpendicular to the beam. This spin reversal effectively changes the sense of the spin precession in the field B_2, which is parallel to B_1, so that without energy transfer due to sample scattering, and if $B_1 l_1 = B_2 l_2$, the net precession angle of each individual neutron at the second $\pi/2$ flipper is zero, independent of the actual number of precessions performed. Therefore at the second $\pi/2$ flipper, all spins refocus to the direction they had at the first $\pi/2$ flipper and they are finally flipped back to the original polarization direction. The quantity one measures with the sample in place is the polarization of the beam at the analyzer, which is the spectral average over all wavelengths

$$P_{NSE} = P_S \cdot \langle \cos\varphi(\lambda) \rangle$$

of the total Larmor precession angle φ. The term cos φ appears because the $\pi/2$ flipper turns only one of the precessing spin components back into the beam direction. P_S takes into account a possible change of the neutron polarization by the scattering itself. In the Section 3. 1. 3 we have seen that nuclear spin-incoherent scattering and magnetic scattering have this effect. Under the condition $\dfrac{B_1 l_1}{\overline{v}_1^3} = \dfrac{B_2 l_2}{\overline{v}_2^3}$, ($\overline{v}_{1,2}$ are the mean neutron velocities in both spectrometer arms), it can be shown that

$$P_{NSE} = \frac{\int S(q,\omega) \cdot \cos(t \cdot \delta\omega) d\omega}{\int S(q,\omega) d\omega} = \frac{I(q,t)}{I(q,0)}$$

with the correlation time ("Fourier time") $t = \dfrac{\gamma \hbar}{m} \cdot \dfrac{B_1 l_1}{\overline{v}_1^3}$. $I(\boldsymbol{q},t)$ is called the intermediate scattering function.

The individual difference precession angles φ are in the first order independent of the actual total number of precessions performed on both sides, which is the reason why one can use a beam with a broad wavelength

distribution, hence with high intensity. It is one of the strong points of NSE that energy resolution and q resolution are decoupled.

If the sample shows dynamics in the spin echo time window, $P(t)$ will decrease as t increases, because the sample scattering introduces a change of the neutron velocity so that the spins do not perfectly refocus at the second $\pi/2$ flipper. However, one has to characterize the response of the spectrometer to an elastic scatterer in order to distinguish between sample dynamics and instrument imperfections which also decrease $P(t)$. Consequently, for each data set P_{NSE}^{sample} (q,t) a second data set $P_{NSE}^{reference}$ (q,t) is required that is measured under identical experimental conditions using an elastic reference sample. Dividing the two data sets P_{NSE}^{sample} (q,t) and $P_{NSE}^{reference}$ (q,t) corresponds exactly to the usual deconvolution of the instrument resolution in the energy domain (as done in triple-axis spectroscopy).

The spin dynamics in magnets are typically quite fast (in the ps range and faster) and not easily observable by spin echo. Another difficulty is that measuring real inelastic modes with spin echo as described here $(\overline{v}_1 \neq \overline{v}_2)$ requires a very complicated spectrometer setup. A way out of this problem is provided by the possible combination of both TAS and NSE, where the spin echo setup is put on top of a host triple-axis spectrometer. This works especially well with the *resonance spin echo* variant (Keller et al., 1998; Köppe et al., 1999, and references therein). In this technique the magnetic precession fields and the $\pi/2$ flippers are replaced by a pair of resonance spin flippers on each spectrometer arm. In a resonance flipper one superposes a high and homogeneous field B_0 and a perpendicular radiofrequency field $B_1\cos(2\pi vt)$. Typically, $v \approx 300$ kHz and $B_0 \approx 100$ G. In such a configuration a π flip is obtained, if the frequency v equals the Larmor frequency of the neutron in the field B_0, and if the amplitude B_1 of the oscillating field is set to

$$B_1 \cdot d = 135.65 \frac{G \cdot cm}{\lambda(\text{Å})}$$ (where d is the flipper thickness). The space between

the flippers is in strictly zero field, hence the spin keeps its direction in the laboratory frame but precesses in the oscillating frame of the flippers.

An example that nicely demonstrates what neutron spin echo can do today is provided by the recent work of Casalta and co-workers (Casalta et al., 1999). They reported an experiment on the spin dynamics of mono-domain iron clusters embedded in an insulating matrix of Al_2O_3. With a mean Fe particle diameter of 20 Å (standard deviation of 4 Å) and a body-centered cubic structure as shown by transmission electron microscopy (TEM), the clusters behave as single-domain particles due to the lack of domain walls. This leads to the existence of a "superspin" associated with the entire particle. Inelastic neutron scattering showed the existence of two distinct magnetic fluctuation components both associated with the whole spin of the particle (superparamagnetic fluctuations). The faster relaxing component could be resolved using triple-axis and time-of-flight spectroscopy and was attributed to transverse fluctuations. The slow component was identified with the longitudinal superspin fluctuations and could be resolved using the ultra-high

energy resolution of the spin echo technique (see Fig. 3. 21). The measurement at a correlation time of 200 ns in this experiment is about equivalent to a measurement at an energy transfer below 10 neV. The increased freezing of the spin dynamics at decreasing temperature and a change in the shape of the correlation function, reflecting a temperature-dependent distribution of individual relaxation times, could be nicely followed in this experiment.

A hot topic in recent magnetism research is the study of "spin-ice" $Ho_2Ti_2O_7$ and related compounds. Here again, only the measurement of the intermediate scattering function $I(q,t)$ which contains all information on the spin dynamics – spatial and temporal – has lead to a real understanding of the magnetic interactions, when combined with what was known using other techniques such as ac-susceptibility and μSR. Spin ice $Ho_2Ti_2O_7$ belongs to the class of *geometrically frustrated* magnets. An extensive introduction into the subject can be found in recent reviews (Ramirez, 2001; Bramwell and Gingras, 2001).
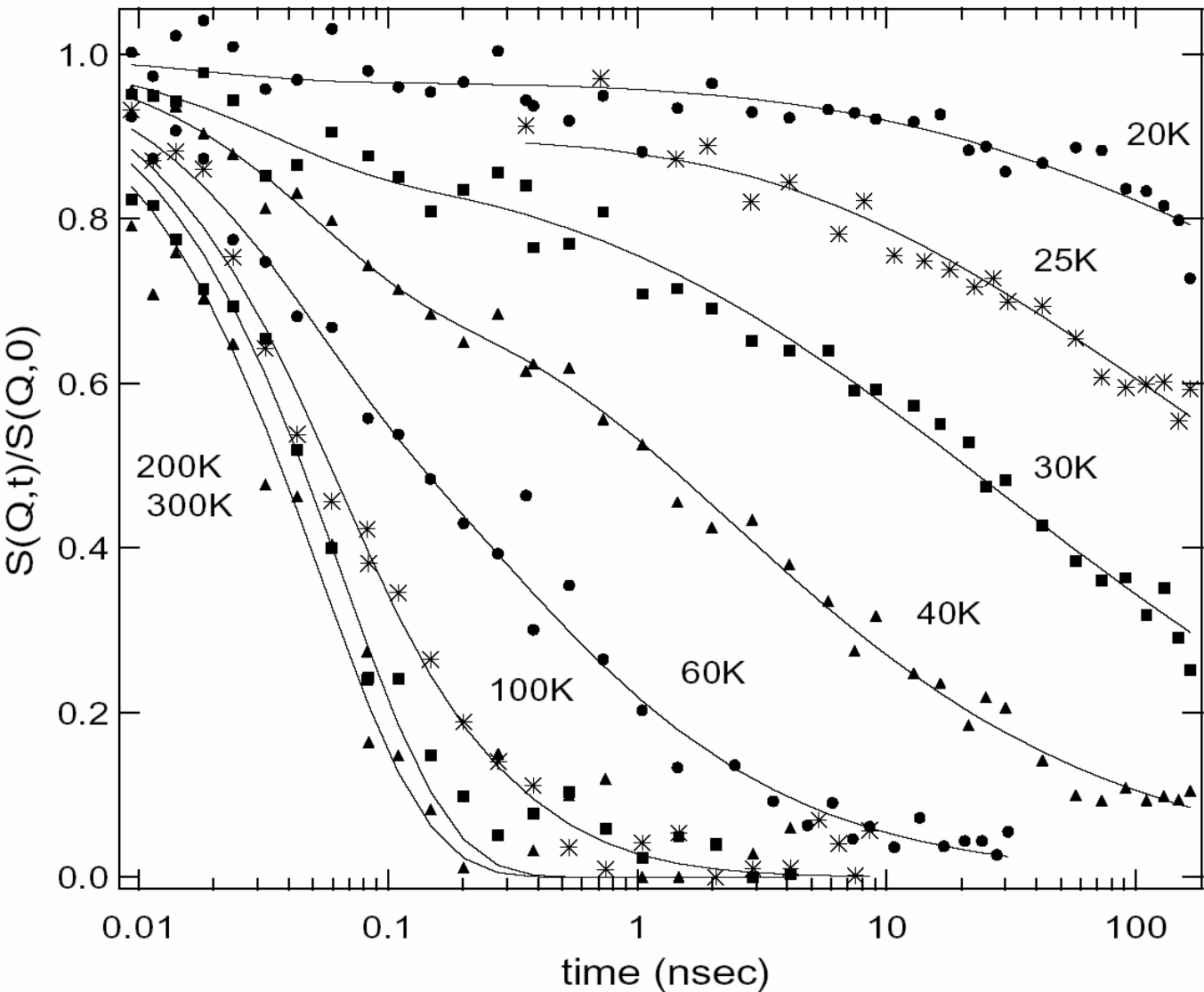

Figure 3. 21   Normalized intermediate scattering function at $q = 0.07\text{Å}^{-1}$ for various temperatures. Below 200 K a specially derived model function is used to fit the data (higher temperature: single exponential relaxation) taking into account a distribution of single relaxation times due to the spread in particle size (Casalta et al., 1999).

The magnetic Ho^{3+} ions occupy a cubic pyrochlore lattice (space group $Fd\bar{3}m$) of corner-linked tetrahedra (see Fig. 3. 22). The magnetic moments are constrained by the crystal electric field (CEF) to local <111> axes. This frustrates the dominant (effectively ferromagnetic) dipolar interactions in the system and leads to frozen, non-collinear, spin disorder below ~1 K. The spin ice state is in a way analogous to the Pauling hydrogen disorder of water ice (H_2O), with each spin equivalent to a hydrogen displacement vector situated on the mid-point of an oxygen-oxygen line of contact. Hence the name spin ice (Harris et al., 1997). The single ion ground state is an almost pure $|J,M_J\rangle = |8,\pm8\rangle$ doublet with <111> quantization axis, separated by over 200 K from the first excited state (Rosenkranz et al., 2000).
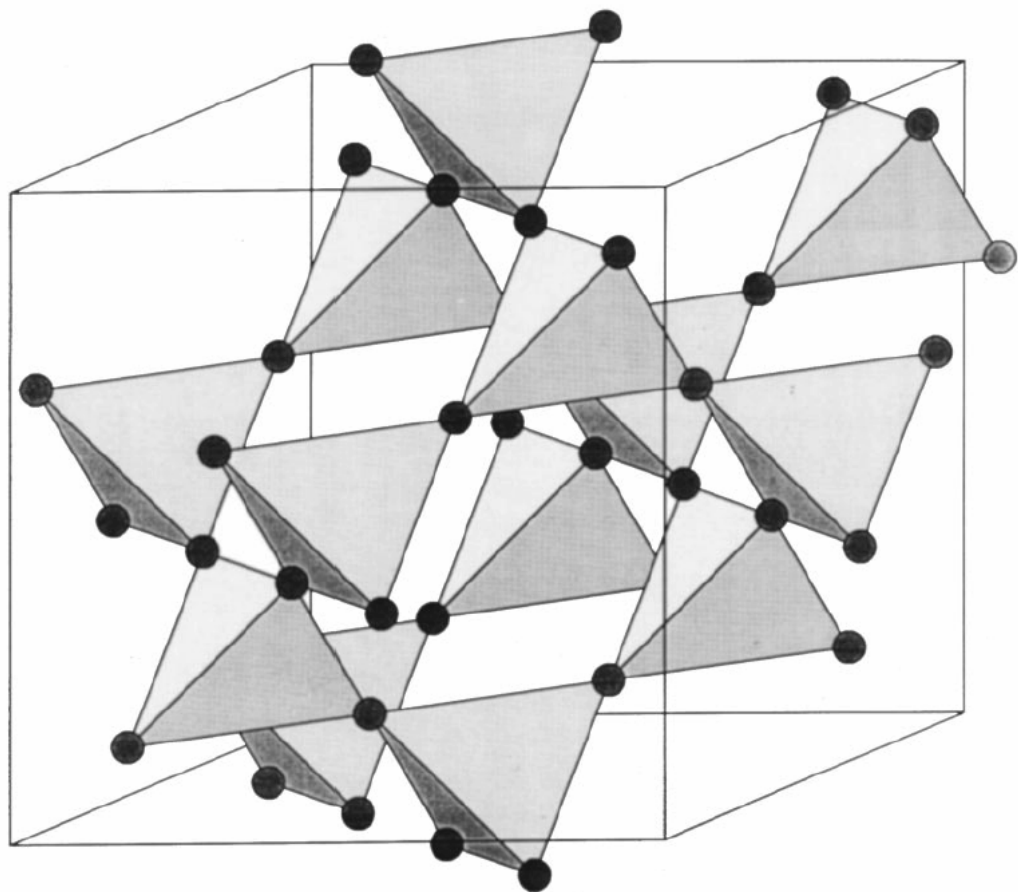

Figure 3. 22　The pryrochlore lattice. In cubic pyrochlores of chemical composition $A_2B_2O_7$ both A and B atom sublattices independently form this network of corner-sharing tetrahedra.

In order to provide a microscopic understanding of ac-susceptibility data, the spin dynamics was investigated using the spin echo technique.

Figure 3. 23 shows the normalized relaxation function $F(q,t) = I(q,t) / I(q,0)$ measured for a polycrystalline sample of $Ho_2Ti_2O_7$ at the IN11 spectrometer (ILL). At all temperatures between 0.05 K and 200 K the relaxation can be fitted with excellent precision to a simple exponential function

$$F(q,t) = A \exp\{-\nu(T)\,t\},$$

where $A = 0.91 \pm 0.01$. The frequency $\nu(T)$ can be fitted to an Arrhenius expression $\nu(T) = 2 \nu_0 \exp(-E_a/k_B T)$ with attempt frequency $\nu_0 = 1.1 \pm 0.2 \times 10^{11}$ Hz and activation energy $E_a = 293 \pm 12$ K. The origin of the dynamics observed in NSE can be identified by the experimental findings: the activation energy is close to the first group of CEF levels (Rosenkranz et al., 2000), and the **q**-independence of the scattering indicates negligible two-spin correlations, so that the dynamics must be due to a single ion spin flip mechanism between the two states of the ground state doublet.

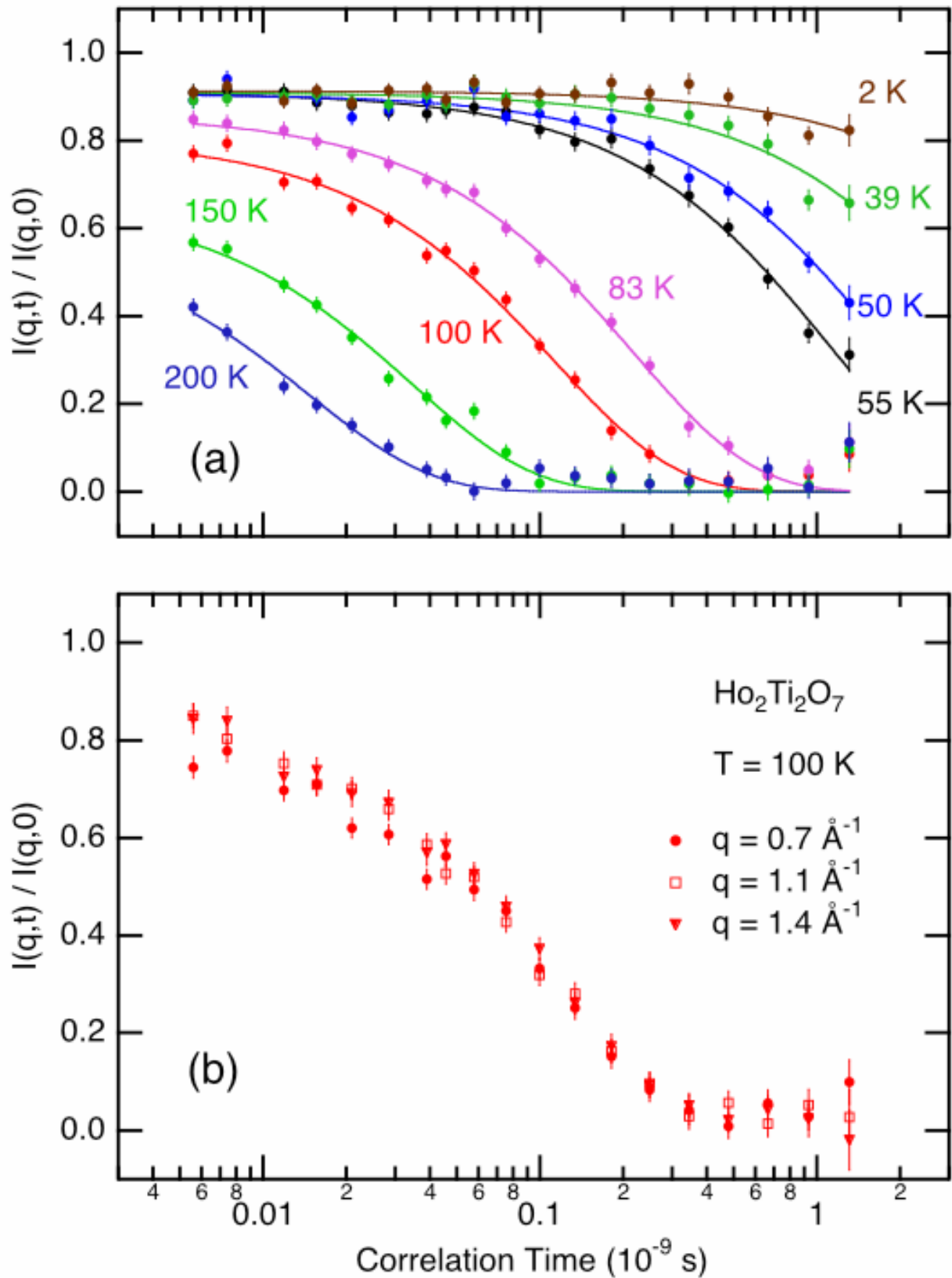
Figure 3. 23   The intermediate scattering function measured for a polycrystalline sample of $Ho_2Ti_2O_7$ at the IN11 spectrometer (ILL). Top panel: at different temperatures showing the speed-up when temperature is increased. Lower panel: at different q's showing the q-independence of the dynamics.

By Fourier transform, the NSE signal can be related to the imaginary part of the generalized susceptibility $\chi''(\boldsymbol{q},\omega)$ which can be extrapolated to $v < 10^5$ Hz for comparison with the bulk ac-susceptibility. This analysis gives

$$\chi(\boldsymbol{q},\omega) = \chi(\boldsymbol{q}) \left\{ \frac{v^2(T)}{v^2(T)+\omega^2} + \frac{i\omega v(T)}{v^2(T)+\omega^2} \right\}$$

where $k_B T \gg \hbar\omega$ was assumed. $\chi(\boldsymbol{q} = 0)$ can be well approximated as $\sim 1/T$ in the relevant temperature range. Inserting $v(T)$ as above one finds that in the ac susceptibility a peak should be observed around 15 K. Such a peak was indeed found (Ehlers et al., 2002) on a single crystal sample of $Ho_2Ti_2O_7$ in finite field. In fact, when χ'' was normalized to $\chi(0)$, it could be seen even in very low field. Its frequency shift implies an activation barrier of ~ 250 K, as expected.

Towards low temperature, the susceptibility was found to increase significantly, though, showing a second peak at ~ 1 K peak associated with an activation energy $E_a' \approx 20$ K and attempt frequency $v_0' \sim 10^{10}$ Hz. This should correspond to a second, even slower dynamical process. It is limited to low temperature (below ~ 15 K) and low frequency, $< 10^5$ Hz (invisible at least in the frequency domain of NSE), and approximately independent of temperature above ~ 4 K. The thermal activation energy of this second process is closer to the other major energy scale in the system: the dipolar interaction, which was estimated to be 2.4 K for spin ice $Ho_2Ti_2O_7$ (Bramwell and Gingras, 2001). Below $T \sim 15$ K, where the spins freeze, they are subject to an unusually strong, slowly fluctuating, dipolar field, created by the nearest neighbors. In a classical picture, near-neighbor spins are fixed along axes at 109.5° to each other, and so experience a mutual torque that cannot be eliminated by local spin reorientation. To explain the very slow dynamics below $T \sim 15$ K, it was therefore suggested that in the temperature range of 4-15 K the transverse component of the dipolar field mixes higher $|M_J\rangle$ states into the ground state, causing the single ion ground state to no longer be an almost pure $|\pm 8\rangle$ doublet, and inducing a finite rate of spin inversion that is temperature-independent. This new "quantum relaxation channel" is only possible in the paramagnetic phase above 1 K where the mean dipolar field is zero.

3. 4   Summaries

Due to its unique elementary characteristics, the neutron is especially suited for probing the magnetic properties of materials. It is not electrically charged, and therefore penetrates deeply into condensed matter. On the other hand, it possesses spin ½, and thus interacts with atomic nuclei as well as with magnetic moments present in matter. These two types of interactions are of

comparable strength. Neutrons with wavelengths in the Å range possess kinetic energies in the meV range, which are the typical energies of elementary excitations in condensed matter. Consequently, neutrons can simultaneously probe structural and magnetic spatial correlations on atomic to mesoscopic length scales, as well as structural and magnetic temporal correlations in the range of 10^{-14} to 10^{-7} s. By keeping track of the neutron spin orientation and its change during the interaction with the sample, one can unambiguously separate nuclear and magnetic scattering processes.

Compared to other experimental techniques developed to investigate magnetic properties of matter, neutron scattering has particular merits: ① transparent and easy experimental procedures that allow a straightforward conversion of experimental data into physical quantities, ② it is a non-destructive technique sensitive to both volume and surface properties, and ③ it is possible to study a huge variety of magnetic phenomena and different classes of materials. The dependence of magnetic properties on temperature, pressure, or magnetic field can easily be explored since most sample environments can be made transparent to neutrons.

We have presented basic instrumental concepts for scattering experiments using spin polarized neutrons, focusing on applications in condensed matter magnetism research. To summarize, an overview on different particular applications for the different techniques is given in the Table 3. 1.

Table 3. 1

	Technique	Applications
Elastic experiments (Structural information)	Powder and single crystal diffraction	Ordering patterns of magnetic moments, magnetization density maps
	Diffuse scattering	Condensed matter: atomic or magnetic short range order, magnetic correlations
	Reflectometry	Magnetization depth profile in thin films, orientation and lateral arrangements of magnetization vectors
	Small angle scattering (SANS)	Investigations on mesoscopic length scales (10 Å to 10000 Å), such as grains or magnetic domains, correlation lengths
Inelastic experiments (Dynamical information)	Triple-axis and chopper spectroscopy	Magnetic excitations (spin waves), phase transitions
	Neutron spin echo	Slow dynamics (e.g. in disordered magnets)

References

Aeppli, G., T. E. Mason, S. M. Hayden, H. A. Mook, J. Kulda, Science **278**, 1432 (1997)

Adams, C. P., J. W. Lynn, Y. M. Mukovskii, A. A. Arsenov, D. A. Shulyatev Phys. Rev. Lett. **85,** 3954 (2000)

Argyriou, D. N., J. W. Lynn, R. Osborn, B. Campbell, J. F. Mitchell, U. Ruett, H. N. Bordallo, A. Wildes, and C. D. Ling, Phys. Rev. Lett. **89**, 036401 (2002)

Als Nielsen, J., in *Topics in Current Physics. Structure and Dynamics of Surfaces* (Springer, Berlin, 1986)

Anderson I.S., B. Hamelin, P. Høghøj, P. Courtois P., H. Humblot, in *Frontiers of Neutron Scattering*, Proc. of the Seventh Summer School on Neutron Scattering, ed. by A. Furrer, (World Scientific, Singapore, 2000)

Ankner, J.F., and G.P. Felcher, J. Magn. Magn. Mater. **200,** 741 (1999)

Baibich, M.N., J.M. Broto, A. Fert, F. Nguyen van Dau, F. Petroff, P. Etienne, G. Creuzet, A. Friedrich, and J. Chazelas, Phys. Rev. Lett. **61**, 2472 (1988)

Boeni, P., J. L. Martinez, J. M. Tranquada, J. Appl. Phys **67,** 5436 (1990)

Boeni, P., D. Clemens, M. Senthil Kumar, C. Pappas, Physica B **267-268**, 320 (1999)

Boucher, J. P., and L. P. Regnault, J. Phys. I France **6**, 1939 (1996)

Bramwell, S. T., and M. J. P. Gingras, Science **294**, 1495 (2001)

Brown, P. J., Physica **B 297**, 198 (2001)

Brown, P. J., J. B. Forsyth, E. Lelievre-Berna, and F. Tasset, J. Phys.: Condens. Matter **14**, 1957 (2002)

Brown, P. J., J. B. Forsyth, and F. Tasset, Physica **B 267-268**, 215 (1999)

Brown, P.J., in *International Tables for Crystallography*, ed. by A.J.C. Wilson, Vol. C, chapter 4.4, (Kluwer Academic Publishers, Dordrecht, 1992) p. 391

Cable, J.W., S. A. Werner, G. P. Felcher, and N. Wakabayashi, Phys. Rev. Lett. **49**, 829 (1982)

Casalta, H., P. Schleger, C. Bellouard, M. Hennion, I. Mirebeau, G. Ehlers, B. Farago, J. - L. Dormann, M. Kelsch, M. Linde, and F. Phillipp, Phys. Rev. Lett. **82**, 1301 (1999)

Coulter K.P., T.E. Chupp, A.B. McDonald, C.D. Bowman, J.D. Bowman, J.J. Szymanski, V. Yuan, G.D. Cates, D.R. Benton, and E.D. Earle, Nucl. Instr. and Meth. **A 288**, 463 (1990)

Cussen, L. D., D. J. Goossens, and T. J. Hicks, Nucl. Instr. Meth. Phys. Res. **A 440,** 409 (2000)

Cywinski, R., S. H. Kilcoyn, and J. R. Stewart, Physica **B 267-268**, 106 (1999)

Desclaux, J. P., and A. J. Freeman, in *Handbook on the Physics and Chemistry of the Actinides*, ed. by A. J. Freeman and G. H. Lander, Vol. 1, (North Holland, Amsterdam, 1984) p. 46

O'Donovan, K.V., J. A. Borchers, C. F. Majkrzak, O. Hellwig, and E. E. Fullerton, Phys. Rev. Lett. **88**, 067201 (2002)

Ehlers, G., A. L. Cornelius, M. Orendác, M. Kajcaková, T. Fennell, S. T. Bramwell, and J. S. Gardner, J. Phys. C Condensed Matter (2002, submitted for publication)

Eilhard, J., A. Zirkel, W. Tschöp, O. Hahn, K. Kremer, O. Schärpf, D. Richter, and U. Buchenau, J. Chem. Phys. **110,** 1819 (1999)

Ewen, B., and D. Richter, *Neutron Spin Echo Investigations on the Segmental Dynamics of Polymers in Melts, Networks and Solutions,* Advances in Polymer Science, Vol. 134, (Springer Verlag, Berlin, Heidelberg, 1997)

Felcher, G.P., and S.G.E. te Velthuis, Appl. Surf. Sci. **182,** 209 (2001)

Freund, A., R. Pynn, W. G. Stirling, and C. M. E. Zeyen, Physica **120B**, 86 (1983)

Fullerton, E.E., J.S. Jiang, and S.D. Bader, J. Mag. Mag. Mater. **200**, 392 (1999)

Furrer, A. (ed.), *Magnetic Neutron Scattering,* Proc. of the Third Summer School on Neutron Scattering, (World Scientific, Singapore, 1995)

Gabrys, B. J., Physica **B 267-268,** 122 (1999)

Garcia-Hernandez, M., F. J. Mompean, O. Schärpf, K. H. Andersen, and B. Fåk, Phys. Rev. B **59,** 958 (1999)

de Gennes, P. G., *Theory of Neutron Scattering by Magnetic Crystals*, in: *Magnetism*, *Vol. 3*, ed. by G. T. Rado, H. Suhl, (Academic Press, New York, 1963)

Groom, D.E. et al., The European Physical Journal **C15**, 1 (2000)

Grünberg, P., R. Schreiber, Y. Pang, M.B. Brodsky, and H. Sowers, Phys. Rev. Lett. **57**, 2442 (1986)

Halpern, O., and M. H. Johnson, Phys. Rev. **55,** 898 (1939)

Harris, M. J., S. T. Bramwell, D. F. McMorrow, T. Zeiske, and K. W. Godfrey, Phys. Rev. Lett. **79**, 2554 (1997)

Hase, M., I. Terasaki, and K. Uchinokura, Phys. Rev. Lett. **70**, 3651 (1993)

Heil, W., J. Dreyer, D. Hofmann, H. Humblot, E. Lelièvre-Berna, and F. Tasset, Physica **B 267-268**, 328 (1999)

Hennion, M., L. Pardi, I. Mirebeau, E. Suard, R. Sessoli, A. Caneschi, Phys. Rev. B **56**, 8819 (1997)

Hayden, S. M., R. Doubble, G. Aeppli, T. G. Perring, E. Fawcett, Phys. Rev. Lett. **84**, 999 (2000)

Hiess, A., P. J. Brown, E. Lelièvre-Berna, B. Roessli, N. Bernhoeft, G. H. Lander, N. Aso, and N. K. Sato, Phys. Rev. **B 64**, 134413 (2001)

Hjörvarsson, B., J.A. Dura, P. Isberg, T. Watanabe, T.J. Udovic, G. Andersson, and C.F. Majkrzak, Phys. Rev. Lett. **79**, 901 (1997)

Hoffmann, A., M. R. Fitzsimmons, J. A. Dura and C. F. Majkrzak, Phys. Rev. B **65**, 024428 (2002)

Kasuya, T., Prog. Theor. Phys. **16**, 45 (1956)

Keller, T., T. Krist, A. Danzig, U. Keiderling, F. Mezei, and A. Wiedenmann, Nucl. Instr. Meth. Phys. Res. **A 451,** 474 (2000)

Keller, T., R. Golub, F. Mezei, R. Gähler, Physica B **241-243**, 101 (1998)

Kiryukhin, V., B. Keimer, J. P. Hill, and A. Vigliante, Phys. Rev. Lett. **76**, 4608 (1996)

Klose, F., Ch. Rehm, D. Nagengast, H. Maletta, and A. Weidinger,
      Phys. Rev. Lett. **78**, 1150 (1997)

Köppe, M., M. Bleuel, R. Gähler, R. Golub, P. Hank, T. Keller, S. Longeville,
      U. Rauch, and J. Wuttke, Physica B **266**, 75 (1999)

Krist, T., F. Klose, and G.P. Felcher, Physica B **248**, 372 (1998)

Lamelas, F.J., S. A. Werner, S. M. Shapiro, and J. A. Mydosh,
      Phys. Rev. **B 51**, 621 (1995)

Lee, S.-H., C.F. Majkrzak, Physica B **267-268**, 341 (1999)

Lee, W.T., and F. Klose, in *Neutron Optics*, ed. by J.L. Wood, I.S. Anderson,
      Proceedings of SPIE Vol. **4509** (2001) p.145

Lee, W.T., F. Klose, H.Q. Yin, and B. P. Toperverg, Physica B (2003),
      accepted for publication

Lee, W.T., S. G. E. te Velthuis, G. P. Felcher, F. Klose, T. Gredig,
      D. Dahlberg, Phys. Rev. **B 65,** 224417 (2002)

Lovesey, S. W., *Theory of Neutron Scattering from Condensed Matter*,
      (Clarendon Press, Oxford, 1984)

Lynn, J. W., N. Rosov, M. Acet, and H. Bach, J. Appl. Phys **75**, 6069 (1994)

Majkrzak, C.F., Physica B, **173,** 75 (1991)

Meneghetti, D., and S. S. Sidhu, Phys. Rev. **105**, 130 (1957)

Mezei, F. (ed.), *Neutron Spin Echo,* Lecture Notes in Physics, Vol. 128,
      (Springer, Berlin, Heidelberg, 1979)

Mezei, F., C. Pappas, and Th. Gutberlet (ed.), *Neutron Spin Echo,* Lecture
      Notes in Physics, Vol. 601, (Springer, Berlin, 2003)

Mezei, F., in *Liquids, Freezing and Glass Transition*, Les Houches, Session
      LI, 1989, ed. by J. P. Hansen, D. Levesque, J. Zinn-Justin, (Elsevier,
      1991)

Mezei, F., *Study of slow dynamical processes by neutron-spin-echo,*
      Int. J. Mod. Phys **B7**, 2885 (1993)

Mezei, F., and P. A. Dagleish, Comm. Phys. **2**, 41 (1977)

Mezei, F., G. Ehlers, C. Pappas, M. Russina, T. J. Hicks, and M. F. Ling,
      Physica **B 276-278**, 543 (2000)

Mook, H.A., Phys. Rev. **148**, 495 (1966)

Moon, R.M. and W. C. Koehler, Phys. Rev. B **11**, 1609 (1975)

Moon, R.M., W. C. Koehler, J. W. Cable, H. R. Child, Phys. Rev. B **5**, 997
      (1972)

Moon, R. M., T. Riste, and W. C. Koehler, Phys. Rev **181**, 920 (1969)

Müller, G., H. Thomas, H. Beck, and J. C. Bonner, Phys. Rev. **B 24**, 1429
      (1981)

Mueller-Buschbaum, P., J.S. Gutmann, R. Cubitt, M. Stamm,
      Colloid Polym. Sci. **277,** 1193 (1999)

Mughabghab, S.F., M. Divadeenam, N.E. Holden, in *Neutron Cross Sections*,
      Vol.1, (Academic Press, New York, 1981)

Murani, A.P., O. Schärpf, K. H. Andersen, D. Richard, and R. Raphel,
      Physica **B 267-268**, 131 (1999)

Nathans, R., C.G. Shull, G. Shirane, A. Andresen,
      J. Phys. Chem. Solids, **10**, 138 (1959)

Parratt, L.G., Phys. Rev. **95,** 359 (1954)

Passell, L. and R.I. Schermer, Phys. Rev. **150**, 146 (1966)

Prinz, G.A., J. Mag. Mag. Mater. **200**, 57 (1999)

Ramirez, A. P., in *Handbook of Magnetic Materials*, ed. by K. H. J. Buschow, Vol. 13, Chapter 4 (Elsevier, Amsterdam, 2001)

Raymond, S., T. Yokoo, A. Zheludev, S. E. Nagler, A. Wildes, and J. Akimitsu, Phys. Rev. Lett. **82**, 2382 (1999)

Regnault, L.P., M. Aïn, B. Hennion, G. Dhalenne, and A. Revcolevschi, Phys. Rev. **B 53**, 5579 (1996)

Regnault, L.P., F. Tasset, J. E. Lorenzo, T. Roberts, G. Dhalenne, and A. Revcolevschi, Physica **B 267-268**, 227 (1999)

Rehm, Ch., F. Klose, D. Nagengast, H. Maletta, and A. Weidinger, Europhys. Lett. **38,** 61 (1997)

Ressouche, E., J. X. Boucherle, B. Gillon, P. Rey, and J. Schweitzer, J. Am. Chem. Soc. **115**, 3610 (1993)

Rich, D.R., S. Fan, T. R. Gentile, D. Hussey, G. L. Jones, B. Neff, W.M. Snow, and A.K. Thompson, Physica B **305,** 203 (2001)

Rosenkranz, S., A. P. Ramirez, A. Hayashi, R. J. Cava, R. Siddharthan, B. S. Shastry, J., Appl. Phys. **87**, 5914 (2000)

Rossat-Mignod, J., *Neutron Scattering*, in: *Methods of Experimental Physics*, Vol.23, ed. by K. Sköld, D. L. Price, (Academic Press, London, 1987)

Ruderman, M.A., and C. Kittel, Phys. Rev **96**, 99 (1954)

Schärpf, O., and H. Capellmann, Phys. Stat. Sol. **A 135**, 359 (1993)

Schreyer, A., C.F. Majkrzak, N.F. Berk, H. Grull, and C.C. Han, J. Phys. Chem. Solids **60,** 1045 (1999)

Shirane, G., S. M. Shapiro, and J. M. Tranquada, *Neutron Scattering with a Triple-Axis Spectrometer*, (Cambridge University Press, Cambridge 2002)

Shull, C.G., W.A. Strauser, and E.O. Wollan, Phys. Rev. **83**, 333 (1951a)

Shull, C.G., E.O. Wollan, W.C. Kohler, Phys. Rev. **84**, 912 (1951b)

Speriosu, V.S., D.A. Herman, Jr., I.L. Sanders, and T. Yohi, IBM J. Res. Develop. **44,** 186 (2000)

Stewart, J. R., K. H. Andersen, R. Cywinski, and A. P. Murani, J. Appl. Phys **87**, 5425 (2000)

Squires, G. L., *Thermal Neutron Scattering*, (Cambridge University Press, Cambridge, 1978)

Tasset, F., P.J. Brown, E. Lelievre-Berna, T. Roberts, S. Pujol, J. Allibon, and E. Bourgeat-Lami, Physica **B 268,** 69 (1999)

Temst K., M.J. Van Bael, and H. Fritzsche, Appl. Phys. Lett. **79**, 991 (2001)

Thompson, D.A., and J.S. Best, IBM J. Res. Develop. **44,** 311 (2000)

Toperverg, B.P., G.P. Felcher, V.V. Metlushko, V. Leiner, R. Siebrecht, and O. Nikonov, Physica **B 283,** 149 (2000)

Toperverg, B.P., Physica **B 297**, 160 (2001)

Wiedenmann, A., Physica B **297**, 226 (2001)

Williams, W. G., *Polarized Neutrons*, (Clarendon Press, Oxford, 1988)

Windsor, C.G., *Pulsed Neutron Scattering*, (Taylor & Francis Ltd., London, and Halsted Press, New York, 1981)

Weissmueller, J., A. Michels, J.G. Barker, A. Wiedenmann, U. Erb,
       and R.D. Shull, Phys. Rev. **B 63,** 214414 (2001)
Yosida, K., Phys. Rev **106**, 893 (1957)
Zabel, H., Physica **B 198,** 156 (1994a)
Zabel, H., Appl. Phys. A – Mater. **58,** 159 (1994b)

Keywords

Cross section formalism

Diffraction

Elastic magnetic scattering

Inelastic neutron scattering

Magnetic scattering

Magnetic excitations

Neutron

Polarization analysis

Polarized neutrons

Polarized neutron instrumentation

Polarized neutron reflectometry

Small-angle neutron scattering

Spin-echo spectroscopy

Supermirrors

Triple-axis spectroscopy

List of Abbreviations and Symbols

A	Ferromagnetic exchange-stiffness constant
AFM	Antiferromagnetic
$\text{Å} = 10^{-10}$ m	(angstrom)
$\boldsymbol{B}$	Magnetic induction vector
b	Bound nuclear coherent scattering length
d	Lattice parameter, length scale, dimension, or grain size
E	Neutron energy
E_a	Activation energy
$F(q)$	Magnetic form factor
$F(q,t)$	Normalized relaxation function (= $I(q,t) / I(q,0)$)
FM	Ferromagnetic
GMR	Giant magnetoresistivity
H	Magnetic field strength
h	Planck's constant
$\hbar$	Planck's constant divided by 2π
$\hat{\boldsymbol{i}}$	Nucleus spin operator
I	Intensity
$I(\boldsymbol{q},t)$	Intermediate scattering function
J	Exchange coupling energy
K	Anisotropy energy coefficient
l	Length
$\boldsymbol{k}$	Neutron wave vector

k_F	Fermi wave vector
k_B	Boltzmann's constant
l_K	Magnetic exchange length
$\boldsymbol{M}$	Magnetization vector
m_n	Neutron mass = 1.675×10^{-27} kg
N_{up} (N_{down})	Number of spin "up" ("down") neutrons in the beam
N	Nucleon number
n	Integer (in Bragg's law)
n	Atomic density
NSE	Neutron spin echo
P	Neutron beam polarization
p	Magnetic scattering length
p_λ	Population factor
PNR	Polarized neutron reflectivity
$\boldsymbol{q}$	Scattering vector (= $\mathbf{k_i} - \mathbf{k_f}$)
R	Reflectivity
$\boldsymbol{r}$	Position vector of a scattering center
r_0	Classical electron radius = 0.282×10^{-12} cm
$\hat{S}$	Polarization tensor
$\hat{S}_i^{\alpha}$	α component of spin operator of an ion at site $\boldsymbol{r}_i$
$S^{\alpha\beta}(\boldsymbol{q},\omega)$	Magnetic scattering function
$\hat{s}$	Neutron spin operator
$\boldsymbol{s}$	Neutron spin vector

SANS	Small-angle neutron scattering
SDW	Spin density wave
SLD	Scattering length density
T	Temperature
T	Relative neutron transmission
T_f	Spin glass temperature
t	Time
TAS	Triple-axis spectroscopy
$\hat{V}$	Interaction potential
$V(z)$	Neutron potential at depth z
v	Velocity
Z	Atomic number
$\gamma/2\pi$	Gyromagnetic ratio of the neutron (= -2916.4 Hz/G)
λ	Neutron wavelength
ν	Frequency (Hz)
$\boldsymbol{\mu}$	Magnetic moment vector
μ_B	Bohr magneton
μ_N	Nuclear magneton (= 5.051 x 10^{-27} J/T)
μ_n	Neutron magnetic moment ($\mu_n = -1.913\mu_N$)
2θ	Scattering angle
θ_C	Critical angle for total reflection of neutrons at surfaces

σ	Cross section (= $4\pi\, b^2$)
Φ	Azimuth angle
φ	Precession angle of neutron spin
χ_{ac}	AC susceptibility
$\chi''(\boldsymbol{q},\omega)$	Generalized susceptibility
χ^2	Magnetic domain dispersion
ω	Angular frequency (rad s^{-1})
ω_L	Larmor frequency
Ω	Solid angle